Geochimica et Cosmochimica Acta 366 (2024) 95–112

Contents lists available at ScienceDirect

Geochimica et Cosmochimica Acta

journal homepage: www.elsevier.com/locate/gca

Dual carbonate clumped isotope (Δ_{47}-Δ_{48}) measurements constrain different sources of kinetic isotope effects and quasi-equilibrium signatures in cave carbonates

Zeeshan A. Parvez [a,b,c,1], Mohammed I. El-Shenawy [d,e,f,1], Jamie K. Lucarelli [b,c,1], Sang-Tae Kim [d], Kathleen R. Johnson [g], Kevin Wright [h], Daniel Gebregiorgis [i], Isabel P. Montanez [j], Barbara Wortham [j], Asfawossen Asrat [k], Eduard Reinhardt [d], John N. Christensen [l], Irvin W. Matamoros [b,c], Joshua Rubi [c,h], Kevin Miguel [c,h], Ben M. Elliott [b,c], Randy Flores [b,c], Shawn Kovacs [d], Robert A. Eagle [c,m,n,o], Aradhna Tripati [b,c,m,n,o,p,q,*]

[a] Department of Chemistry and Biochemistry, University of California, Los Angeles, CA, USA
[b] Department of Earth, Planetary, and Space Sciences, University of California, Los Angeles, CA, USA
[c] Center for Diverse Leadership in Science, University of California, Los Angeles, CA, USA
[d] School of Earth, Environment, & Society, McMaster University, Hamilton, ON, Canada
[e] Institut für Geologie und Mineralogie, Universität zu Köln, 50674 Köln, Germany
[f] Department of Geology, Beni-Suef University, Beni-Suef 62511, Egypt
[g] Department of Physical Sciences, University of California, Irvine, CA, USA
[h] East Los Angeles College, Los Angeles, CA, USA
[i] Department of Geosciences, Georgia State University, Atlanta, GA, USA
[j] Department of Earth and Planetary Sciences, University of California, Davis, CA, USA
[k] Department of Mining and Geological Engineering, Botswana International University of Science and Technology, Palapye, Botswana
[l] Department of Energy Geosciences, Lawrence Berkeley National Laboratory, Berkeley, CA, USA
[m] Department of Atmospheric and Oceanic Sciences, University of California, Los Angeles, CA, USA
[n] Institute of Environment and Sustainability, University of California, Los Angeles, CA, USA
[o] School of Earth Sciences, University of Bristol, United Kingdom
[p] Institute of Geophysics and Planetary Physics, University of California, Los Angeles, CA, USA
[q] California Nanosystems Institute, University of California, Los Angeles, CA, USA

ARTICLE INFO

Associate editor: Ruth E. Blake

Keywords:
Speleothems
Clumped isotopes
Cave carbonates

ABSTRACT

Cave carbonate minerals are an important terrestrial paleoclimate archive. A few studies have explored the potential for applying carbonate clumped isotope thermometry to speleothems as a tool for constraining past temperatures. To date, most papers utilizing this method have focused on mass-47 clumped isotope values (Δ_{47}) at a single location and reported that cave carbonate minerals rarely achieve isotopic equilibrium, with kinetic isotope effects (KIEs) attributed to CO_2 degassing. More recently, studies have shown that mass-47 and mass-48 CO_2 from acid digested carbonate minerals (Δ_{47} and Δ_{48}) can be used together to assess equilibrium and probe KIEs. Here, we examined 44 natural and synthetic modern cave carbonate mineral samples from 13 localities with varying environmental conditions (ventilation, water level, pCO_2, temperature) for (dis)equilibrium using Δ_{47}-Δ_{48} values, in concert with traditional stable carbon ($\delta^{13}C$) and oxygen ($\delta^{18}O$) isotope ratios. Data showed that 19 of 44 samples exhibited Δ_{47}-Δ_{48} values indistinguishable from isotopic equilibrium, and 18 (95 %) of these samples yield Δ_{47}-predicted temperatures within error of measured modern temperatures. Conversely, 25 samples exhibited isotopic disequilibria, 13 of which yield erroneous temperature estimates. Within some speleothem samples, we find Δ_{47}-Δ_{48} values consistent with CO_2 degassing effects, however, the majority of samples with KIEs are consistent with other processes being dominant. We hypothesize that these values reflect isotopic buffering effects on clumped isotopes that can be considerable and cannot be overlooked. Using a Raleigh

* Corresponding author at: Department of Earth, Planetary, and Space Sciences, University of California, Los Angeles, CA, USA.
E-mail address: atripati@g.ucla.edu (A. Tripati).
[1] Joint first author.

https://doi.org/10.1016/j.gca.2023.11.017
Received 28 April 2023; Accepted 22 November 2023
Available online 27 November 2023

Distillation Model, we examined carbon and oxygen isotope exchange trajectories and their relationships with dual clumped isotope disequilibria. Carbon isotope exchange is associated with depletion of both Δ_{47} and Δ_{48} relative to equilibrium, while oxygen isotope exchange is associated with enrichment of both Δ_{47} and Δ_{48} relative to equilibrium. Cave rafts collected from proximate locations in Mexico exhibit the largest average departures from equilibrium ($\overline{\Delta\Delta_{47}} = -0.032 \pm 0.007$, $\overline{\Delta\Delta_{48}} = -0.104 \pm 0.035$, where $\Delta\Delta_i$ is the measured value – the equilibrium value). This study shows how the Δ_{47}-Δ_{48} dual carbonate clumped isotope framework can be applied to a variety of tcave carbonate mineral samples, enabling identification of isotopic equilibria and therefore quantitative application of clumped isotope thermometry for paleoclimate reconstruction, or alternatively, constraining the mechanisms of kinetic effects.

1. Introduction

Speleothems have been widely used as terrestrial paleoclimate archives (Bar-Matthews et al., 1997; Wang et al., 2001, 2004a,b; Burns et al., 2003; Fleitmann et al., 2003). This is due to annual cave temperatures remaining relatively constant (±1 °C) and reflecting the mean annual air temperature of the region (Poulson and White, 1969; McDermott, 2004; McDermott et al., 2011). Additionally, cave carbonate minerals can be accurately dated with U-series dating methods (Richards, 2003; McDermott, 2004; Scholz and Hoffmann, 2008). Oxygen isotope ratios are the most commonly studied temperature proxy applied to speleothems used for paleoclimatology, and are based on a temperature-dependent relationship of the oxygen isotope fractionation factor (α) between carbonate minerals and water (Kim and O'Neil, 1997). However, quantitative interpretation of oxygen isotope ratios in terrestrial carbonate minerals is hampered by the lack of constraints on the isotopic composition of waters, and on the magnitude of disequilibrium isotope effects. The complex isotopic evolution of meteoric water as it passes through the surface atmosphere, soil, karst zones, and adjusted cave atmospheric zone poses a challenge for accurate application of this paleothermometer (Dreybrodt, 2012; McDermott, 2004; Lachniet, 2009). In addition, fractionation associated with prior calcite precipitation and isotopic exchange between CO_2 in the cave atmosphere further complicate the use of this proxy (Mickler et al., 2006; Dreybrodt et al., 2016; Hansen et al., 2017, 2022). In modern samples, this can be circumvented by controlled studies where the traditional isotopic compositions of cave drip waters are monitored at the approximate time and location of precipitation. In older speleothems, the potential for variation through time complicates reconstructions.

Other temperature proxies have also been used in speleothems to varying degrees of success, including Mg/Ca and alkenone unsaturation indexes as indirect proxies (Bar-Matthews et al., 2003; Almogi-Labin et al., 2009), analyzing isoprenoid tetraether (TEX_{86}) (Powers et al., 2004; Tierney et al., 2008), fluid inclusion micro thermometry (Krüger et al., 2011; Meckler et al., 2015), fluid inclusion stable isotope analysis (Van Breukelen et al., 2008; Dennis et al., 2011; Affolter et al., 2014), noble gas thermometry (Kluge et al., 2008; Scheidegger et al., 2011; Ghadiri et al., 2018), and clumped isotope paleothermometry (Ghosh et al., 2006; Schauble et al., 2006; Affek et al., 2008; Meckler et al., 2015; Kluge et al., 2014; Daëron et al., 2019). The first study of clumped isotopes in speleothems showed that kinetic effects can impart a substantial bias (Affek et al., 2008), which has more recently been revisited (Matthews et al., 2021).

The foundation of clumped isotope thermometry is the thermodynamic equilibrium-driven preference of heavy isotope aggregation (Wang et al., 2004a,b; Eiler and Schauble, 2004; Ghosh et al., 2006; Schauble et al., 2006; Eiler, 2007). Most clumped isotope studies have focused on measuring the relative abundance of the multiply substituted isotopologue of CO_2 with a mass of 47 ($^{13}C^{18}O^{16}O$ – Δ_{47}), derived from acid digestion of carbonate minerals. However, one of the major caveats in Δ_{47}-thermometry is the underlying assumption that dissolved inorganic carbon (DIC) achieves isotopic equilibrium prior to mineral precipitation (Ghosh et al., 2006). Isotopic disequilibria for bulk $\delta^{18}O$ and $\delta^{13}C$ are observed in cave monitoring studies and synthetic precipitation experiments. These studies have reported speleothem fractionation factors that are between kinetic and equilibrium endmember values (Tremaine et al., 2011; Day and Henderson, 2011; Johnston et al., 2013; Hansen et al., 2019; El-Shenawy et al., 2020). A widely utilized test for probing oxygen isotopic disequilibria in speleothems is the Hendy Test (Hendy, 1971). However, this test is not universally applicable to all cave carbonates because it does not account for covariation in $\delta^{18}O$ and $\delta^{13}C$, and disequilibrium $\delta^{18}O$ values that may occur within different growth intervals (Dorale and Liu, 2009). Further, the Hendy Test has not yet been evaluated in depth for clumped isotopes.

Some cave carbonates are thought to have formed in clumped isotope equilibrium based on modern samples that yield Δ_{47}-temperatures that accurately reflect annual temperature, including Pleistocene speleothem samples from Borneo that were used to infer glacial-interglacial temperature changes (Meckler et al., 2015) and the slow growing speleothems of Devils Hole (Kluge et al., 2014; Tripati et al., 2015; Daëron et al., 2019; Bajnai et al., 2020, 2021; Lucarelli et al., 2023a,b) and Corchia Caves (Daëron et al., 2019). In other cave carbonate samples, empirical observations suggest CO_2 degassing causes an increase in $\delta^{18}O$ and a decrease in Δ_{47} (Daëron et al., 2011; Kluge and Affek, 2012; Affek and Zaarur, 2014).

The paired or dual carbonate clumped isotope (Δ_{47} and Δ_{48}) system can provide another method for probing clumped isotopic disequilibria (Tripati et al., 2015; Bajnai et al., 2020; Guo, 2020) including in cave carbonates (Bajnai et al., 2021). Recent advancements in mass spectrometry have enabled the measurement of the less abundant mass 48 isotopologue ($^{12}C^{18}O^{18}O$–Δ_{48}) at sufficient precision for such applications (Fiebig et al., 2019; Bajnai et al., 2020; Lucarelli et al., 2023a). Dual clumped isotope measurements of Δ_{47} and Δ_{48} have been theoretically and experimentally shown to have an equilibrium relationship and constrained boundaries for disequilibrium trajectories in DIC pools and carbonate minerals. These relationships can be used to identify the origin of kinetic effects, the extent of deviation from equilibrium, and timescales associated with carbonate and mineral evolution (Hill et al., 2014; Tripati et al., 2015; Fiebig et al., 2019, 2021; Guo, 2020; Bajnai et al., 2020, 2021; Lucarelli et al., 2023a,b; Parvez et al., 2023). Bajnai et al. (2021) and Lucarelli et al. (2023a) successfully used dual clumped isotope space to assess equilibrium conditions associated with modern and Pleistocene Devil's Hole vein and mammillary calcite samples and confirmed consistent temperature over the past 570 ka.

Here, we have brought together a wide suite of cave carbonate samples from 13 localities, both natural and synthetic, produced in diverse growth environments (e.g., cave ventilation and temperature). These samples were selected to systematically explore factors influencing dual carbonate clumped isotopes (Δ_{47}, Δ_{48}) and traditional stable isotopes ($\delta^{13}C$ and $\delta^{18}O$) in caves. We examined if the dual clumped isotope method can determine which samples accurately predict modern temperatures. For samples with disequilibrium isotopic values, we then used dual clumped isotopes in concert with traditional stable isotopes to investigate the magnitude and mechanism of disequilibria.

2. Background

2.1. Cave systems

Meteoric water seeps through various subsurface zones prior to entering cave systems. These zones typically include soil, epikarst, and within-cave atmosphere environments. Meteoric water has a low pCO_2 and its oxygen and carbon isotope composition are governed by the hydrological cycle and atmospheric CO_2 (Dansgaard, 1964; Craig and Gordon, 1965). Upon entry into soil, the meteoric water is introduced to an environment which generally has a higher pCO_2 that forces an equilibration of CO_2 dissolved in the water (Dreybrodt and Scholz, 2011). Subsequently, this acidic water dissolves the carbonate minerals as it percolates through the epikarst zone below the soil. In this environment, the bulk isotopic composition of carbon is dictated by environmental factors. An example of which is the shift in $\delta^{13}C$ values of carbonate minerals precipitated in soil caused by decaying vegetation. C3 plants generally induce a –14 to –6 ‰ shift in $\delta^{13}C$, whereas C4 plants induce a –6 to +2 ‰ shift (McDermott, 2004). In contrast, the oxygen isotope composition of percolating water initially preserves the isotopic signature of the meteoric water because of the relatively large oxygen reservoir in meteoric water compared to respired CO_2 in soil and DIC in epikarst (Dreybrodt and Scholz, 2011). Finally, the percolating water (high pCO_2 and pH of 5) enters the cave either as a water drop or a flowing thin film which are then exposed to the low pCO_2 cave atmosphere. The partial pressure gradient of the pCO_2 between the cave atmosphere and the percolating (drip) water triggers CO_2 degassing and $CaCO_3$ precipitation out of the drip water (reaction (1)).

$$Ca^{2+}(aq) + 2HCO_3^-(aq) \rightarrow CaCO_3(s) + H_2O(aq) + CO_2(g) \quad (1)$$

The CO_2 degassing results in an increase in pH from around 5.0 to 8.9, based on whether the cave is an open or closed system (Dreybrodt, 2012). This leads DIC speciation to be approximately 96 % HCO_3^- (Tripati et al., 2015). The rate of CO_2 degassing in caves increases with decreasing thickness of the flowing water film (Hansen et al., 2022). Fast CO_2 degassing leads to progressive carbonate precipitation out of isotopic equilibrium with cave water (El-Shenawy et al., 2020). For example, fast CO_2 degassing isotopically enriches the remaining DIC species in cave water, and consequently the precipitated carbonates are relatively enriched in ^{13}C and ^{18}O due to the preferential escape of $^{12}C^{16}O_2$ (Mühlinghaus et al., 2009; Scholz and Hoffmann, 2008). However, slow CO_2 degassing allows enough time for cave water to buffer the isotopic enrichment in the DIC species and facilitates the precipitation of carbonate at or close to isotope equilibrium (El-Shenawy et al., 2020). In addition to fast CO_2 degassing, isotope exchange between the DIC species in water and atmospheric CO_2 in well-ventilated caves can cause disequilibrium isotope effects in the precipitated carbonates (Dreybrodt et al., 2016; Hansen et al., 2017). In particular, carbon isotope exchange between atmospheric CO_2 and DIC in water in well-ventilated caves enriches the DIC species in ^{13}C and thereby the precipitated carbonates (Dreybrodt et al., 2016).

2.2. Carbonate Clumped Isotope Geochemistry and Notation

There are 20 different isotopologues of C O_3^{2-} with four that are singly-substituted, meaning they contain either a single heavy isotope of carbon or oxygen. The singly substituted variants make up ~1.8 % of the total abundance (Eiler and Schauble, 2004; Eiler, 2007). The remaining 16 isotopologues are multiply substituted "clumped" isotopes that contain ≥2 heavy isotopes of carbon and/or oxygen (Ghosh et al., 2006). Reactions (2) and (3) show isotope exchange reactions that form the multiply substituted isotopologues with *m/z* 63 ($^{13}C^{18}O^{16}O^{16}O$) and *m/z* 64 ($^{12}C^{18}O^{18}O^{16}O$), with the clumped species indicated in bold.

$$[^{12}C^{16}O^{18}O^{16}O]^{2-} + [^{13}C^{16}O^{16}O^{16}O]^{2-} \leftrightarrow [^{12}C^{16}O^{16}O^{16}O]^{2-} + \mathbf{[^{13}C^{16}O^{18}O^{16}O]^{2-}} \quad (2)$$

$$[^{12}C^{16}O^{18}O^{16}O]^{2-} + [^{12}C^{18}O^{16}O^{16}O]^{2-} \leftrightarrow [^{12}C^{16}O^{16}O^{16}O]^{2-} + \mathbf{[^{12}C^{18}O^{18}O^{16}O]^{2-}} \quad (3)$$

The temperature-dependent equilibrium constant for reactions (2) and (3) are the basis of the carbonate clumped isotope thermometer (Ghosh et al., 2006; Schauble et al., 2006).

No current method allows for the direct measurement of clumped isotopes in carbonate minerals. Thus, *m/z* 63 and *m/z* 64 carbonate ions within the mineral are converted to gaseous *m/z* 47 and *m/z* 48 CO_2, respectively, and measured in a gas-source isotope-ratio mass spectrometer (Ghosh et al., 2006) using the relationships in equations (4) and (5):

$$\Delta_{47} = \left[\left(\frac{R_{47}}{R_{47}^*} - 1\right) - \left(\frac{R_{46}}{R_{46}^*} - 1\right) - \left(\frac{R_{45}}{R_{45}^*} - 1\right)\right] \times 1000 \quad (4)$$

$$\Delta_{48} = \left[\left(\frac{R_{48}}{R_{48}^*} - 1\right) - 2\left(\frac{R_{46}}{R_{46}^*} - 1\right)\right] \times 1000 \quad (5)$$

where R_i and R_i^* represent the measured and stochastic ratios of i/44 isotopologues, respectively (Wang et al., 2004a,b; Eiler and Schauble, 2004; Ghosh et al., 2006; Schauble et al., 2006; Eiler, 2007).

The time required for DIC in an aqueous solution to achieve clumped and oxygen isotope equilibrium is controlled by the forward and reverse rate constants for reactions (6)–(12) (Zeebe and Wolf-Gladrow, 2001; Beck et al., 2005; Tripati et al., 2015; Guo, 2020; Uchikawa et al., 2021; Watkins and Devriendt, 2022):

$$CO_2 + H_2O \leftrightarrow H_2CO_3 \leftrightarrow HCO_3^- + H^+ \quad (6)$$

$$CO_2 + OH^- \leftrightarrow HCO_3^- \quad (7)$$

$$HCO_3^- + OH \leftrightarrow H_2O + CO_3^{2-} \quad (8)$$

$$HCO_3^- \leftrightarrow H^+ + CO_3^{2-} \quad (9)$$

$$H_2O \leftrightarrow H^+ + OH^- \quad (10)$$

$$Ca^{2+} + HCO_3^- \leftrightarrow CaCO_3(s) + H^+ \quad (11)$$

$$Ca^{2+} + CO_3^{2-} \leftrightarrow CaCO_3(s) \quad (12)$$

Once CO_2 is dissolved in an aqueous solution, it undergoes (de)hydration or (de)hydroxylation reactions, leading to the formation of HCO_3^- (reactions (6) and (7)). These two reactions are the most important in $^{18}O/^{16}O$ isotopic equilibration as they provide the only route for the direct exchange of O atoms in the DIC-H_2O system (Zeebe and Wolf-Gladrow, 2001). Reactions (8)–(10) show the pathway from HCO_3^- to CO_3^{2-} and splitting of water molecules, and reactions (11) and (12) result in carbonate mineral formation. The time needed for DIC and H_2O to isotopically equilibrate is dependent on pH and temperature (Beck et al., 2005), and can impact clumped isotope values (Tripati et al., 2015).

Disequilibrium clumped isotope values have been measured in most Earth-surface carbonate minerals (Daëron et al., 2019). Biominerals such as brachiopod shells (Carpenter and Lohmann, 1995; Bajnai et al., 2018; Rollion-Bard et al., 2019) and coral skeletons (McConnaughey, 1989; Cohen, 2003; Rollion-Bard et al., 2010; Thiagarajan et al., 2011; Saenger et al., 2012; Kimball et al., 2016; Spooner et al., 2016) are hypothesized to have biological effects that cause disequilibrium fractionation. In abiotic carbonate minerals, KIEs associated with (de)hydration and (de)hydroxylation reactions can cause departures from isotopic equilibrium (Ghosh et al., 2006; Guo, 2009, 2020; Saenger et al., 2012; Falk et al., 2016; Spooner et al., 2016; Parvez et al., 2023). In high pH lab experiments, Tang et al. (2014) observed Δ_{47} values that were enriched relative to equilibrium in calcite (precipitated at pH ≥ 10). This phenomenon has been hypothesized to have occurred due to insufficient time for the DIC pool to achieve isotopic equilibrium prior to mineral precipitation (Tang and Feng, 2001; Tripati et al., 2015). At

elevated pH, the [CO_2] available to participate in isotopic equilibration reactions (6) and (7) is extremely low, where ~99 % of DIC is CO_3^{2-} at pH ≥ 10 (Beck et al., 2005; Hill et al., 2014; Tripati et al., 2015).

Speleothems are known to exhibit non-equilibrium clumped isotope effects due to CO_2 degassing (Affek et al., 2008; Daëron et al., 2011; Kluge and Affek, 2012; Fiebig et al., 2019; Guo and Zhou, 2019; Guo, 2020; Bajnai et al., 2020). CO_2 degassing is predicted to lead to an enrichment of $\delta^{18}O$ and Δ_{48} values, accompanied by a depletion in Δ_{47} values (Daëron et al., 2011; Kluge and Affek, 2012; Fiebig et al., 2019; Guo and Zhou, 2019; Guo, 2020; Bajnai et al., 2020). In some cases, speleothems exhibit a Δ_{47}-reconstructed temperature bias of ~10 °C or more when compared to mineral formation temperatures (Kluge et al., 2013).

3. Materials and methods

3.1. Sample collection and information

Speleothems were collected from 13 localities shown in Fig. 1 and described in Table 1. Here, we compiled these samples, which are modern natural and synthetic speleothems that grew in environments with varying ventilation, water levels, and temperature. A brief description of each site is provided below, and reported $\delta^{18}O_{water}$ values for each sample are given in Table S1. Additional details on collection method, recovery protocols, and processing are given in the respective citations.

3.1.1. Cenote Rainbow, Feno, and Monkey Dust, Mexico samples

Cave raft samples were collected from 3 cave systems located in the Yucatan Peninsula and are described in Kovacs et al. (2018). The cave systems are referred to as Cenote Rainbow, Feno, and Monkey Dust. Each cave had a different profile exposed to the atmosphere and water levels which fluctuated following seasonal trends. Samples R1, R2, R3, and R5 were collected from Cenote Rainbow. The Cenote Rainbow cave system is 2.2 km inland (20°29′52.44″N, 87°15′29.65″W) from the Caribbean Sea coast, and is situated in between the townships of Puerto Aventuras and Akumal. This cenote is an extension of the X'tabay cave system that is 1,394 m in length and 13.7 m in depth, and is considered well ventilated, with one side open to the atmosphere. The water level of the cave fluctuated from 0.34 m to 0.94 m. Samples F1, F2, F3, F4, and F5 were collected from Cenote Feno. The Cenote Feno cave is located north of Tulum (20°19′17.34″N, 87°25′43.91″W) and is part of the Sistema Fenomeno cave system and is considered a closed system, with only a small opening to outside atmosphere. The water level of this cave fluctuated from 0.31 m to 0.98 m. Samples B1, B3, and B5 were collected from Cenote Monkey Dust, also known as Cenote Borge. The Cenote Monkey Dust is located south of Tulum (20°11′19.81″N, 87°33′4.66″W) and is part of the Sistema Dos Pisos cave system and is completely open to atmosphere, and considered well ventilated. The water level of this cave fluctuated from 0.41 m to 1.15 m.

3.1.2. Cueva Bonita, Mexico samples

Farmed calcite plates and naturally occurring speleothem samples were collected by Wright et al. (2022) from Cueva Bonita (23°N, 99°W; 1071 m above sea level) located in the northern-most tropical cloud forest of Sierra Madre Oriental in the Northeast state of Tamaulipas. The farmed calcite plates include samples CB-D6, CB-D62, CB3, CB4-Scar, and CB4-Scar2. The speleothem (stalagmite) samples include CB4-12-Wet, CB4-48-Dry, CB4-82-Wet, CB4-99-Dry, and CB4-Top which are samples drilled from the central growth axis of the CB4 stalagmite (Wright et al., 2022). Farmed calcite plates were collected using frosted glass plates that were placed under cave drip water for a period of ~6 months to 1 year.

3.1.3. Cueva de la Puente, Mexico samples

Farmed calcite plates were recovered from Cueva de la Puente in San

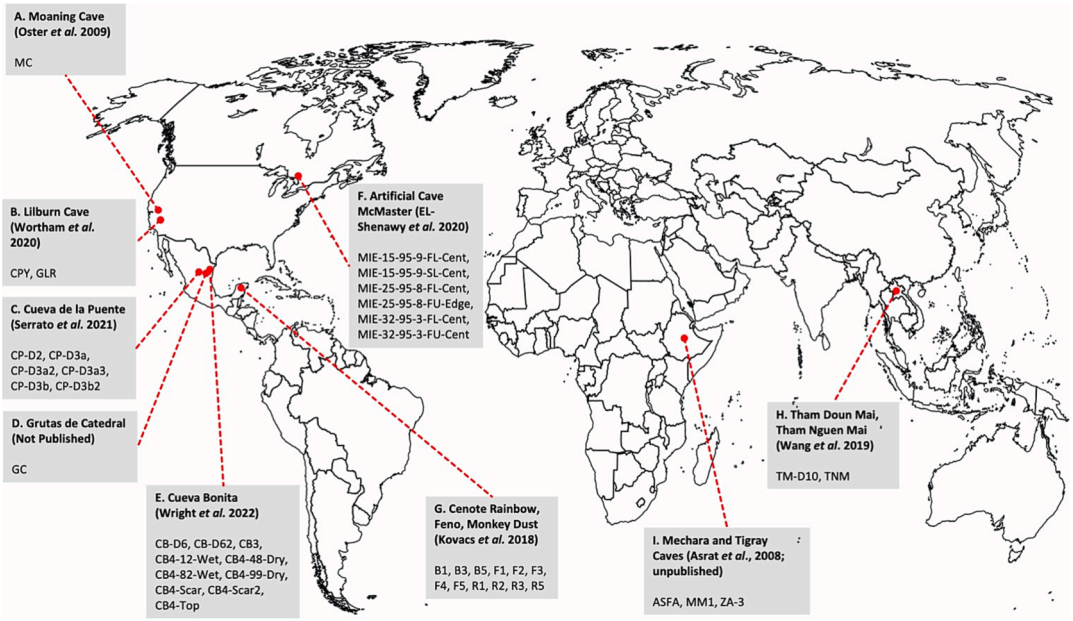

Fig. 1. Map showing cave sample localities and names of individual samples recovered, which were measured for Δ_{47} and Δ_{48} as part of this study. Citations below indicate studies where caves are described. (A) Moaning Cave, California, USA. Samples: Moaning Cave (MC; Oster et al., 2009). (B) Liliburn Cave, California, USA. Samples: Canopy (CPY) and Glacier (GLR; Wortham et al., 2021). (C) Cueva de la Puente, Mexico. Samples: CP-D2, CP-D3a, CP-D3a2, CP-D3a3, CP-D3b, and CP-D3b2 (Serrato Marks et al., 2021). (D) Grutas de Catedral, Mexico. Sample: GC (Not Published). (E) Cueva Bonita, Mexico. Samples: CB-D6, CB-D62, CB3, CB4-12-Wet, CB4-48-Dry, CB4-82-Wet, CB4-99-Dry, CB4-Scar, CB4-Scar2, and CB4-Top (Wright et al., 2022). (F) Artificial Cave, McMaster, Canada. Samples: MIE-15-95-9-FL-Cent, MIE-15-95-9-SL-Cent, MIE-25-95-8-FL-Cent, MIE-25-95-8-FU-Edge, MIE-32-95-3-FL-Cent, and MIE-32-95-3-FU-Cent (El-Shenawy et al. 2020). (G) Cenote (Rainbow, Feno, Monkey Dust), Mexico. Samples: B1, B3, B5, F1, F2, F3, F4, F5, R1, R2, R3, and R5 (Kovacs et al., 2018). (H) Tham Doun Mai and Tham Nguen Mai, Laos. Samples: TM-D10 and TNM (Wang et al., 2019). (I) Mechara and Tigray Caves, Ethiopia, Africa. Samples: ASFA, MM1, ZA-3 (Asrat et al., 2008; unpublished).

Table 1
Sample information including sample names, type, recovery location, recovery dates, and citation source. Unpublished information associated with samples GC and TNM was provided by co-author Kathleen Johnson; and ASFA was provided by co-author Daniel Gebregiorgis.

Sample Name	Sample Type	Location	Recovery Dates	Source Citation
B1	Cave Raft	Monkey Dust (Borge) Cenote, Mexico	May 2014–May 2016	Kovacs et al. (2018)
B3	Cave Raft	Monkey Dust (Borge) Cenote, Mexico	May 2014–May 2016	
B5	Cave Raft	Monkey Dust (Borge) Cenote, Mexico	May 2014–May 2016	
F1	Cave Raft	Feno Cenote, Mexico	May 2014–May 2016	
F2	Cave Raft	Feno Cenote, Mexico	May 2014–May 2016	
F3	Cave Raft	Feno Cenote, Mexico	May 2014–May 2016	
F4	Cave Raft	Feno Cenote, Mexico	May 2014–May 2016	
F5	Cave Raft	Feno Cenote, Mexico	May 2014–May 2016	
R1	Cave Raft	Rainbow Cenote, Mexico	May 2014–May 2016	
R2	Cave Raft	Rainbow Cenote, Mexico	May 2014–May 2016	
R3	Cave Raft	Rainbow Cenote, Mexico	May 2014–May 2016	
R5	Cave Raft	Rainbow Cenote, Mexico	May 2014–May 2016	
CB-D6	Farmed Calcite Plate	Cueva Bonita, Mexico	May 2018–May 2020	Wright et al. (2022)
CB-D62	Farmed Calcite Plate	Cueva Bonita, Mexico	May 2019–Feb 2020	
CB3	Farmed Calcite Plate	Cueva Bonita, Mexico	Jan 2017–Jan 2018	
CB4-Scar	Farmed Calcite Plate	Cueva Bonita, Mexico	May 2018–May 2019	
CB4-Scar2	Farmed Calcite Plate	Cueva Bonita, Mexico	May 2019–Feb 2020	
CB4-12-Wet	Speleothem	Cueva Bonita, Mexico	June 2018–May 2019	
CB4-48-Dry	Speleothem	Cueva Bonita, Mexico	June 2018–May 2019	
CB4-82-Wet	Speleothem	Cueva Bonita, Mexico	June 2018–May 2019	
CB4-99-Dry	Speleothem	Cueva Bonita, Mexico	June 2018–May 2019	
CB4-Top	Speleothem	Cueva Bonita, Mexico	June 2018–May 2019	
CP-D2	Farmed Calcite Plate	Cueva de la Puenta, Mexico	Apr 2017–May 2018	Serrato (2020)
CP-D3a	Farmed Calcite Plate	Cueva de la Puenta, Mexico	May 2018–May 2019	
CP-D3a2	Farmed Calcite Plate	Cueva de la Puenta, Mexico	May 2019–Nov 2019	
CP-D3a3	Farmed Calcite Plate	Cueva de la Puenta, Mexico	Nov 2019–Feb 2020	
CP-D3b	Farmed Calcite Plate	Cueva de la Puenta, Mexico	May 2018–May 2019	
CP-D3b2	Farmed Calcite Plate	Cueva de la Puenta, Mexico	May 2019–Nov 2019	
GC	Farmed Calcite Plate	Grutas de Catedral, Mexico	Apr 2017–May 2018	Kathleen Johnson
TM-D10	Farmed Calcite Plate	Tham Doun Mai, Laos	Feb 2015–Feb 2017	Wang et al. (2019); Griffiths et al. (2020)
TNM	Farmed Calcite Plate	Tham Nguen Mai, Laos	Jan 2019–Feb 2020	Kathleen Johnson
CPY	Farmed Calcite Plate	Liburn Cave, California, United States	May 2018–Feb 2020	Wortham et al. (2021)
GLR	Farmed Calcite Plate	Liburn Cave, California, United States	May 2018–Feb 2020	
Moaning Cave	Speleothem	Moaning Cave, California, United States	Mar 2006–Jul 2009	Oster et al. (2009)
MIE-15–95-9-FL-Center	Artificial Speleothem	McMaster University, Ontario, Canada	N/A	El-Shenawy et al. (2020)
MIE-15–95-9-FU-Edge	Artificial Speleothem	McMaster University, Ontario, Canada	N/A	
MIE-15–95-9-SL-Center	Artificial Speleothem	McMaster University, Ontario, Canada	N/A	
MIE-25–95-8-FL-Center	Artificial Speleothem	McMaster University, Ontario, Canada	N/A	
MIE-25–95-8-FU-Edge	Artificial Speleothem	McMaster University, Ontario, Canada	N/A	
MIE-32–95-3-FL-Center	Artificial Speleothem	McMaster University, Ontario, Canada	N/A	
MIE-32–95-3-FU-Center	Artificial Speleothem	McMaster University, Ontario, Canada	N/A	
ASFA	Speleothem	Mechara Caves, Ethiopia, Africa	April 2004–September 2007	Asrat et al. (2008)
MM1	Speleothem	Tigray Caves, Ethiopia, Africa	N/A	Daniel Gebregiorgis
ZA-3	Speleothem	Tigray Caves, Ethiopia Africa	N/A	

Luis Potosi, Mexico (21.98°N, 100.57°W) by Serrato (2020). The cave is located at an elevation of 2,109 m above sea level and the local geology is dominated by upper Cretaceous fluorite-rich limestone with thin soil cover.

3.1.4. Lilburn Cave, California, United States samples

Farmed calcite samples Glacier and Canopy were recovered by Wortham et al. (2021) from the Lilburn Caves in Sequoia and Kings Canyon National Park located in Central California. Glacier (GLR) was recovered from a site located 30 m away from the surface entrance to the cave system. Canopy (CPY) was recovered further away from the surface entrance at 61 m. Sanded watch glasses of approximately 10 cm in diameter were positioned under an active drip from which new calcite grew from 2018 to 2020.

3.1.5. Moaning Cave, California, United States samples

Speleothems were collected by Oster et al. (2009) from the Moaning Cave (38.06°N, 120.46°W) located in the California Sierra Nevada mountain range. The samples were collected through core sampling of a stalagmite where the drip center was well defined. U-series dating indicates the core formed during the Holocene. The piece used here was sourced from the top of the core, and therefore likely formed over a few hundred years, with the youngest portion being ~450 years old.

3.1.6. Tham Doun Mai Cave, Laos samples

Samples were collected from the Tham Doun Mai Cave (20°45′N, 102°38′E) by Wang et al. (2019) and Griffiths et al. (2020), and are labeled TM-D10 in our study. This cave is ~3,745 m long and located 352 m above sea level in Luang Prabang Province, Laos. Core samples of the stalagmites located ~200 m from the entrance of the cave were taken for analysis.

3.1.7. Tham Nguen Mai Cave, Laos samples

The sample TNM was collected by Kathleen Johnson from the Tham Nguen Mai cave located in Khammouane Province, Laos. The cave is 2,189 m long and located upstream from the Xe Bang Fai sink and is likely part of an ancient underground route of the Xe Bang Fai River. Farmed calcite plates were collected from under an active drip approximately 300 m from the cave entrance. These calcite plates were farmed between January 2019 and March 2020.

3.1.8. McMaster Artificial Cave samples

Synthetic speleothem samples were grown in an artificial cave that simulated cave drip and stalagmite growth by El-Shenawy et al. (2020). A pure $CaCO_3$ saturated solution with a pCO_2 level of 14,000–18,000 parts per million by volume (ppmv) was distributed to a 35 cm long Pyrex tube channel (e.g., stalactite) that allowed for CO_2 degassing to occur before the water impinges the upper watch glass (e.g., stalagmite) at a distance of 85 cm, and then flow to the lower watch glass (e.g., pool). The solution was injected into the long tube at 3 different flow rates (fast, intermediate, and slow). The environment in this cave system was controlled with temperature being modulated between 15, 25, and 32 °C; relative humidity at 95 %; and a pCO_2 of ~550 ppmv. Samples MIE-15-95-9-FL-Cent, MIE-15-95-9-FU-Edge, MIE-15-95-9-SL-Cent, MIE-25-95-8-FL-Cent, MIE-25-95-8-FU-Edge, MIE-32-95-3-FL-Cent, and MIE-32-95-3-FU-Cent were precipitated from this artificial cave.

3.1.9. Mechara and Tigray Caves, Ethiopian Highlands samples

Sample ASFA was collected from Rukiessa cave in the Mechara cave system, located in the Southeastern Ethiopian Highlands, and are described by Asrat et al. (2008). The Rukiessa cave's entrance is 1 km east of the eastern bank of the Mechara river (09°51′N, 37°65′E, elevation: 1618 m ASL). The cave is regularly flushed by seasonal floods which contain allogenic sediments. The entrance is a 2 m deep vertical hole in a sandy limestone layer that opens to a few chambers in a vertical series. The third chamber, known as the Asfa Chamber, approximately 30 m below the surface is where stalagmite sample ASFA was collected. This chamber is described as very wet, with pool waters fed by drips from active stalactites, and percolation-fed streams (Asrat et al., 2008).

Sample MM1 was collected from May Mekden cave (13°34′58″N, 39°34′5″E). It is a small 3 m long cave at the side of a cliff with the stalagmite collected near the entrance of the cave. MM-1 is not from a dripping cave, so no drip water isotope information is available. The ZA-3 sample was collected from Zayei cave (13°33'26"N, 39°08'44"E). Zayei cave is a 330 m long, 50-60 m wide (at its mid-section) and 10 m high chamber formed into a dripping, wet and humid (within cave temperature is 25 °C; relative humidity is 88%; Asrat et al., 2009). It is decorated with numerous speleothems. Both caves are located within the Jurassic limestone formations in the Tigray region of northern Ethiopia.

3.2. Isotopic Analyses and Instrumentation

All isotopic measurements were made in the Eagle-Tripati clumped isotope laboratory using a common acid bath (CAB) system coupled with a Nu Instruments Perspective IS isotope ratio mass spectrometer (IRMS) from 2020 to 2022, using methods from Upadhyay et al. (2021), Lucarelli et al. (2023a), and Parvez et al. (2023). Clumped isotope measurements were performed on evolved CO_2 produced by digestion of 0.5 mg of $CaCO_3$ samples in phosphoric acid at 90 °C. CO_2 was cryogenically purified in a cold finger and an Adsorption Trap (AdTrap) packed with Porapak Type-Q^{TM} 50/80 and silver wool. Following purification, the sample CO_2 gas is transferred to the IRMS system. This instrument operates entirely under vacuum pressure and does not use a carrier gas. The laboratory CAB-IRMS systems have been shown to yield accurate and reproducible Δ_{47} (Upadhyay et al., 2021; Lucarelli et al., 2023a) and Δ_{48} data (Lucarelli et al., 2023a), with standards that agree with published values from other labs for Δ_{47} (Bernasconi et al., 2021) and Δ_{48} (Bajnai et al., 2020; Swart et al., 2021). The Nu Perspective IRMS is optimized for clumped isotope analysis with secondary electron suppression. Energy filters and quadratic lenses fitted in front of the Faraday collectors for m/z 47–49 drives the suppression. The detectors for m/z 44, 45, and 46 are registered through $3x10^8$, $3x10^{10}$, and $3x10^{11}$ Ω resistors, respectively. The detectors for m/z 47, 48, and 49 are registered through $3x10^{12}$ Ω resistors. A dual-inlet system allows for the input of the sample gas and a reference gas controlled by a bellows system that inputs both through a changeover block, so the sample and reference gases can be compared in real-time. The bellow system has 4 blocks of 15 cycles, for a total of 60 cycles of sample to standard comparison, with an 8-second changeover delay and 20 s of integration per cycle, for a total integration time of 1,200 s. There are continuous pressure adjustments to achieve 80 nA (24 V) on m/z 44 at every acquisition (Upadhyay et al., 2021; Lucarelli et al., 2023a).

3.3. Standardization and Data Processing

The CO_2 reference gas used was sourced from Oztech with an isotopic composition of $\delta^{18}O_{V\text{-}SMOW} = 24.9$ ‰; $\delta^{13}C_{V\text{-}PDB} = -3.56$ ‰. Data was processed and corrected using Easotope 64-bit, release version 20201231 (John and Bowen, 2016) with IUPAC parameters (Brand et al., 2010; Daëron et al., 2016). The Δ_{47} values are reported in the Intercarb-Carbon Dioxide Equilibrium Scale (I-CDES) (Bernasconi et al., 2021) and Δ_{48} values are reported in the Carbon Dioxide Equilibrium Scale (CDES90) (Fiebig et al., 2019; Lucarelli et al., 2023a), meaning the Δ_{47} and Δ_{48} values are presented relative to standards with an acid digestion temperature of 90 °C. No acid fractionation factor (AFF) was applied to Δ_{47} or Δ_{48} data. The raw Δ_{47} and Δ_{48} values were corrected with an empirical transfer function (ETF) and nonlinearity correction, following methods from Dennis et al. (2011). The carbonate standards used in Δ_{47} and Δ_{48} ETFs include Carmel Chalk, CMTile, ETH-1, ETH-2, ETH-3, ETH-4, and Veinstrom (Upadhyay et al., 2021; Lucarelli et al., 2023a). International standards ETH-1 and ETH-2 were used to make

nonlinearity corrections for both raw δ^{47} versus Δ_{47} and δ^{48} versus Δ_{48} data. All sample and standard replicate values are reported in a file repository given the Data Availability section. The standard mean values and reproducibility of Δ_{47}, Δ_{48}, $\delta^{18}O$, and $\delta^{13}O$ are reported in Table S2.

All samples, except for sample CB4-12-Wet, had a minimum of 3 replicates. The number of sample replicates was dictated by the amount of sample provided and the robustness of standard replicate data for standards measured within the same correction interval as the sample. The sample CB4-12-Wet had insufficient material for 3 replicate analyses, and is denoted with a gray symbol in all figures. In figures and tables, the 68 % (1 standard error; SE) and 95 % confidence interval (CI) are indicated.

3.4. Modeling of the DIC-H_2O-CO_2 System Using IsoDIC

To illustrate the evolution of isotopic values in the DIC pool, specifically HCO_3^- and CO_3^{2-}, we used the IsoDIC modeling software developed by Guo and Zhou (2019) and Guo (2020). This modeling software predicts kinetic isotope fractionation in clumped isotopes in a DIC-H_2O-CO_2 system. It simulates reactions (6)–(10) for the evolution of isotopologue reactions involving all major isotopes of C and O, equating to a total of 155 reactions. The forward and reverse rate constants were estimated using Eq. (13) below,

$$k^* = \alpha_{KIE} k \quad (13)$$

where k is the rate constant of the isotopically non-substituted reactions, and α_{KIE} is the kinetic isotope fractionation factor for the isotopically substituted reaction. The product of these variables yields k*, the modified rate constant for the isotopically substituted reaction. (De) hydration and (de)hydroxylation reactions, reactions (6) and (7), are the only reactions that contribute to isotopic fractionation. The interconversion between HCO_3^- and CO_3^{2-} and the splitting of water molecules, reactions (8)–(10), are assumed to be at equilibrium due to their relatively rapid rates of reaction (Guo and Zhou, 2019; Guo, 2020). The equations used by this model are described in the Supplementary Material, and in depth in Guo (2020).

The following parameters were input into the IsoDIC model to determine isotopic evolution during CO_2 absorption and degassing: Degassing (1) solution temperature = 25.0 °C, (2) solution pH = 8, (3) air pCO_2 = 300 ppm, (4) $\delta^{13}C_{V\text{-}PDB}$ air = −10.00 ‰, (5) $\delta^{18}O_{V\text{-}SMOW}$ air = 41.46 ‰ (6) system evolution time = 12 h, (7) clumped isotope temperature (T) = 25.0 °C; Absorption (1) solution temperature = 25.0 °C, (2) solution pH = 9, (3) air pCO_2 = 3,000 ppm, (4) $\delta^{13}C_{V\text{-}PDB}$ air = −10.00 ‰, (5) $\delta^{18}O_{VSMOW}$ air = 41.46 ‰, (6) system evolution time = 12 h, (7) clumped isotope T = 25.0 °C. These values do not correlate to a specific cave or environment and are default parameters used by Guo (2020).

The model yields Δ_{63} and Δ_{64} values which were converted into Δ_{47} and Δ_{48} values using acid fractionation factors (AFFs; y) determined in Lucarelli et al. (2023a) in Eqs. (14) and (15).

$$\Delta_{47} = \Delta_{63} + y \quad (14)$$

$$\Delta_{48} = \Delta_{64} + y \quad (15)$$

An AFF of y = 0.196 ‰ was used for the conversion of Δ_{63} to Δ_{47}, and an AFF of y = 0.131 ‰ was used for the conversion of Δ_{64} to Δ_{48}. These AFFs account for the temperature-dependent removal of ^{16}O versus ^{18}O during acid digestion of carbonate minerals (Guo et al., 2009).

3.5. Determination of disequilibrium versus equilibrium samples

Samples were considered to have achieved equilibrium if their Δ_{47}-Δ_{48} values were indistinguishable from equilibrium, meaning equilibrium Δ_{47}-Δ_{48} values were within the 95 % CI of the measured values. We also calculated $\Delta\delta^{18}O$, $\Delta\Delta_{47}$, and $\Delta\Delta_{48}$ by taking the difference between measured values and equilibrium values calculated for the respective conditions for each cave. Equilibrium $\delta^{18}O$ values were calculated for the various caves using the reported temperature (see Section 2.1 for references) and $\delta^{18}O_{water}$, in conjunction with the temperature-dependent fractionation factors determined by Kim and O'Neil (1997), with the caveat that there may be seasonal variation in $\delta^{18}O_{water}$. The Δ_{47} and Δ_{48} equilibrium values were calculated with respect to reported cave temperatures using relationships from Anderson et al. (2021) and Lucarelli et al. (2023a).

4. Results

4.1. Δ_{47}, Δ_{48}, $\delta^{13}C$, and $\delta^{18}O$ analyses

All isotopic data are reported in Table 2. The Δ_{47} and Δ_{48} values versus $\delta^{18}O$ and $\delta^{13}C$ values with respect to sample type are plotted in Figs. 2 and 3, respectively. In the text below, we report the ranges of measured isotopic values for each sample location that has >1 collected sample. Plots of Δ_{47} and Δ_{48} versus $\delta^{13}C$ and $\delta^{18}O$ with all samples aggregated are reported in Fig. S2.

4.1.1. Cave rafts

The Δ_{47}, Δ_{48}, $\delta^{18}O$, and $\delta^{13}C$ values for the cave rafts from 3 proximate cenotes, Rainbow, Feno, and Monkey Dust, (samples: B1, B3, B5, F1, F2, F3, F4, F5, R1, R2, R3, R5), collected by Kovacs et al. (2018), range from 0.550 ‰ to 0.610 ‰, 0.075 ‰ to 0.237 ‰, 24.6 ‰ to 25.3 ‰, and −11.8 ‰ to −9.5 ‰, respectively.

4.1.2. Farmed calcite plates

The Δ_{47}, Δ_{48}, $\delta^{18}O$, and $\delta^{13}C$ values for the farmed calcite plates from Cueva Bonita (CB-D6, CB-D62, CB3, CB4-Scar, CB4-Scar2), collected by Wright et al. (2022), range from 0.601 ‰ to 0.634 ‰, 0.237 ‰ to 0.289 ‰, 25.7 ‰ to 26.8 ‰, and −12.9 ‰ to −5.3 ‰, respectively. The Δ_{47}, Δ_{48}, $\delta^{18}O$, and $\delta^{13}C$ values for the farmed calcite from Cueva de la Puenta (CP-D2, CP-D3a, CP-D3a2, CP-D3a3, CP-D3b, CP-D3b2), collected by Serrato (2020), range from 0.579 ‰ to 0.639 ‰, 0.139 ‰ to 0.288 ‰, 21.5 ‰ to 22.2 ‰, and −10.8 ‰ to −8.5 ‰, respectively. The Δ_{47}, Δ_{48}, $\delta^{18}O$, and $\delta^{13}C$ values for farmed calcite from Lilburn Cave (CPY, GLR), collected by Wortham et al. (2021), range from 0.640 ‰ to 0.645 ‰, 0.201 ‰ to 0.266 ‰, 22.1 ‰ to 22.5 ‰, and −8.7 ‰ to −9.7 ‰, respectively.

4.1.3. Speleothems

The Δ_{47}, Δ_{48}, $\delta^{18}O$, and $\delta^{13}C$ values for the speleothem samples from Cueva Bonita (CB4-12-Wet, CB4-48-Dry, CB4-82-Wet, CB4-99-Dry, CB4-Top), collected by Wright et al. (2022), range from 0.591 ‰ to 0.618 ‰, 0.226 ‰ to 0.334 ‰, 25.5 ‰ to 26.9 ‰, and −11.0 ‰ to −7.4 ‰, respectively. The Δ_{47}, Δ_{48}, $\delta^{18}O$, and $\delta^{13}C$ values for the synthetic speleothem samples (MIE-15-95-9-FL-Center, MIE-15-95-9-FU-Edge, MIE-15-95-9-SL-Center, MIE-25-95-8-FL-Center, MIE-25-95-8-FU-Edge, MIE-32-95-3-FL-Center, MIE-32-95-3-FU-Center), synthesized by El-Shenawy et al. (2020), range from 0.564 ‰ to 0.629 ‰, 0.171 ‰ to 0.353 ‰, 20.1 ‰ to 24.3 ‰, and −29.0 ‰ to −15.4 ‰ respectively.

4.2. Isotopic Disequilibrium Analysis ($\Delta\Delta_{47}$, $\Delta\Delta_{48}$, and $\Delta\delta^{18}O$)

The difference between measured sample values and calculated equilibrium values for clumped (Lucarelli et al., 2023a) and oxygen isotopes (Kim and O'Neil, 1997) was determined based on the respective cave conditions, and reported in Table 3. The majority of samples, 40 out of 44 (91 %) did not have equilibrium $\Delta\delta^{18}O$ values (Fig. 4). However, 19 of 44 samples (48 %), were within the 95 % CI of $\Delta\Delta_{48}$ versus $\Delta\Delta_{47}$ equilibrium (the origin in Fig. 5). All cave raft samples except one had significant depletions in Δ_{47} and Δ_{48} values relative to equilibrium (Fig. 5). Additional plots of aggregated sample $\Delta\Delta_{47}$, $\Delta\Delta_{48}$, and $\Delta\delta^{18}O$ values are in Figs. S3 and S4. In the text below, we report the ranges of

Table 2
Clumped and bulk isotope data for all samples measured in this study.

Sample Name	# of replicates	$\delta^{13}C_{V\text{-}PDB}$ (‰)	1 SE	95 % CI	$\delta^{18}O_{V\text{-}PDB}$ (‰)	1 SE	95 % CI	$\Delta_{47\ I\text{-}CDES}$ (‰)	1 SE	95 % CI	$\Delta_{48\ CDES90}$ (‰)	1 SE	95 % CI
B1	3	−10.98	0.01	0.02	−5.72	0.12	0.23	0.550	0.007	0.014	0.075	0.033	0.065
B3	5	−10.71	0.00	0.01	−5.77	0.02	0.05	0.566	0.013	0.026	0.161	0.034	0.067
B5	5	−11.04	0.03	0.05	−6.01	0.07	0.13	0.573	0.005	0.009	0.193	0.016	0.032
F1	4	−11.43	0.02	0.04	−5.72	0.03	0.06	0.570	0.004	0.007	0.135	0.026	0.051
F2	5	−11.51	0.06	0.12	−5.70	0.02	0.04	0.610	0.018	0.035	0.237	0.046	0.090
F3	5	−11.66	0.04	0.08	−5.73	0.05	0.09	0.589	0.007	0.015	0.190	0.018	0.035
F4	5	−11.01	0.02	0.05	−6.04	0.11	0.22	0.574	0.010	0.020	0.182	0.014	0.027
F5	4	−11.38	0.07	0.13	−5.97	0.10	0.20	0.584	0.005	0.010	0.207	0.008	0.015
R1	3	−10.35	0.08	0.15	−5.49	0.05	0.09	0.587	0.020	0.040	0.114	0.019	0.038
R2	4	−11.79	0.04	0.08	−6.12	0.02	0.04	0.579	0.010	0.020	0.195	0.019	0.038
R3	5	−9.53	0.06	0.11	−5.43	0.09	0.17	0.564	0.012	0.023	0.150	0.031	0.060
R5	5	−10.08	0.04	0.08	−5.59	0.08	0.16	0.565	0.012	0.023	0.137	0.022	0.044
CB-D6	5	−9.92	0.02	0.05	−5.02	0.04	0.08	0.634	0.017	0.034	0.289	0.015	0.028
CB-D62	4	−9.92	0.02	0.03	−5.04	0.02	0.04	0.601	0.010	0.020	0.239	0.020	0.039
CB3	4	−5.33	0.00	0.00	−4.00	0.03	0.05	0.602	0.015	0.029	0.237	0.019	0.037
CB4-Scar	5	−12.87	0.03	0.05	−4.82	0.03	0.05	0.627	0.015	0.029	0.275	0.033	0.065
CB4-Scar2	5	−12.22	0.02	0.04	−5.02	0.05	0.09	0.623	0.023	0.044	0.274	0.029	0.056
CB4-12-Wet	2	−10.31	0.03	0.06	−5.24	0.00	0.01	0.607	0.002	0.003	0.238	0.061	0.119
CB4-48-Dry	6	−9.46	0.01	0.02	−4.02	0.02	0.05	0.618	0.014	0.028	0.334	0.038	0.075
CB4-82-Wet	4	−9.81	0.01	0.03	−4.79	0.04	0.07	0.613	0.016	0.032	0.226	0.036	0.071
CB4-99-Dry	5	−7.41	0.06	0.12	−3.90	0.07	0.13	0.606	0.013	0.026	0.240	0.032	0.063
CB4-Top	4	−11.04	0.05	0.09	−4.92	0.02	0.03	0.591	0.017	0.033	0.295	0.033	0.064
CP-D2	6	−10.80	0.15	0.29	−9.17	0.04	0.09	0.623	0.029	0.057	0.196	0.036	0.070
CP-D3a	5	−8.80	0.17	0.34	−8.49	0.11	0.21	0.595	0.022	0.044	0.139	0.026	0.051
CP-D3a2	5	−8.65	0.09	0.18	−8.61	0.07	0.14	0.610	0.024	0.048	0.205	0.026	0.050
CP-D3a3	5	−10.38	0.20	0.38	−9.10	0.09	0.17	0.639	0.008	0.016	0.288	0.034	0.068
CP-D3b	4	−8.51	0.02	0.04	−8.45	0.04	0.08	0.579	0.008	0.015	0.239	0.029	0.058
CP-D3b2	5	−9.85	0.13	0.26	−8.98	0.10	0.20	0.618	0.018	0.035	0.198	0.018	0.035
GC	5	−10.54	0.11	0.21	−7.10	0.09	0.17	0.641	0.014	0.028	0.285	0.018	0.035
TM-D10	5	−14.45	0.03	0.06	−8.83	0.04	0.09	0.603	0.008	0.016	0.318	0.027	0.053
TNM	5	−14.75	0.05	0.09	−9.46	0.06	0.11	0.632	0.021	0.042	0.314	0.019	0.038
CPY	5	−9.72	0.02	0.04	−8.57	0.02	0.04	0.645	0.008	0.016	0.266	0.018	0.035
GLR	4	−8.68	0.05	0.09	−8.19	0.03	0.06	0.640	0.012	0.024	0.201	0.009	0.018
Moaning Cave	5	−8.23	0.04	0.07	−7.92	0.02	0.05	0.600	0.006	0.011	0.292	0.034	0.067
MIE-15-95-9-FL-Center	4	−24.30	0.03	0.06	−6.82	0.01	0.01	0.612	0.005	0.009	0.214	0.036	0.070
MIE-15-95-9-FU-Edge	4	−27.80	0.05	0.10	−6.94	0.02	0.05	0.616	0.009	0.017	0.353	0.012	0.023
MIE-15-95-9-SL-Center	5	−15.43	0.10	0.20	−6.40	0.01	0.02	0.629	0.005	0.010	0.292	0.030	0.059
MIE-25-95-8-FL-Center	5	−23.31	0.02	0.04	−9.01	0.01	0.02	0.596	0.005	0.010	0.242	0.017	0.034
MIE-25-95-8-FU-Edge	8	−28.80	0.03	0.07	−8.59	0.02	0.04	0.569	0.011	0.021	0.286	0.031	0.060
MIE-32-95-3-FL-Center	5	−20.73	0.02	0.04	−10.53	0.01	0.02	0.564	0.012	0.024	0.171	0.015	0.028
MIE-32-95-3-FU-Center	7	−29.04	0.03	0.05	−9.74	0.02	0.04	0.578	0.005	0.010	0.217	0.031	0.062
ASFA	6	−7.41	0.01	0.01	−1.14	0.02	0.03	0.610	0.008	0.016	0.167	0.032	0.063
MM1	6	−4.18	0.00	0.01	−2.81	0.02	0.03	0.591	0.004	0.007	0.194	0.026	0.050
ZA-3	6	−0.48	0.01	0.02	−6.18	0.01	0.03	0.610	0.005	0.010	0.210	0.023	0.045

calculated disequilibria for each sample location that has >1 collected sample.

4.2.1. Cave rafts

The $\Delta\Delta_{47}$, $\Delta\Delta_{48}$, and $\Delta\delta^{18}O$ ranges for the cave rafts collected from Cenote Feno, Rainbow, and Monkey Dust, in Mexico (Kovacs et al., 2018) are −0.045 ‰ to 0.014 ‰, −0.172 ‰ to 0.010 ‰, and −0.9 ‰ to 1.2 ‰, respectively.

4.2.2. Farmed calcite

The $\Delta\Delta_{47}$, $\Delta\Delta_{48}$, and $\Delta\delta^{18}O$ values of the calcite plates farmed by Wright et al. (2022) from Cueva Bonita, Mexico range from −0.013 ‰ to 0.019 ‰, −0.017 ‰ to 0.035 ‰, and −0.1 ‰ to 1.3 ‰, respectively. The $\Delta\Delta_{47}$, $\Delta\Delta_{48}$, and $\Delta\delta^{18}O$ values of the calcite plates farmed by Serrato (2020) from Cueva de la Puente, Mexico range from −0.033 ‰ to 0.032 ‰, −0.115 ‰ to 0.037 ‰, and −0.3 ‰ to 0.8 ‰, respectively. The $\Delta\Delta_{47}$, $\Delta\Delta_{48}$, and $\Delta\delta^{18}O$ values of the calcite plates farmed by Wortham et al. (2021) from Lilburn Cave, California, USA range from −0.006 ‰ to −0.002 ‰, −0.068 ‰ to −0.003 ‰, and 1.3 ‰ to 1.7 ‰, respectively.

4.2.3. Speleothems

The $\Delta\Delta_{47}$, $\Delta\Delta_{48}$, and $\Delta\delta^{18}O$ values for the CB4 speleothem subsamples from Cueva Bonita, Mexico, collected by Wright et al. (2022), range from −0.022 ‰ to 0.003 ‰, −0.028 ‰ to 0.080 ‰, and 0.0 ‰ to 1.3 , respectively. The $\Delta\Delta_{47}$, $\Delta\Delta_{48}$, and $\Delta\delta^{18}O$ for the artificial speleothem samples synthesized by El-Shenawy et al. (2020) range from −0.025 ‰ to 0.005 ‰, −0.067 ‰ to 0.095 ‰, and −0.1 ‰ to 1.8 ‰, respectively.

5. Discussion

5.1. Assessing disequilibria of cave carbonates using traditional stable isotopes ($\delta^{13}C$ and $\delta^{18}O$)

Carbonate minerals in cave environments are mainly formed via CO_2 degassing out of waters saturated with respect to calcite which is caused

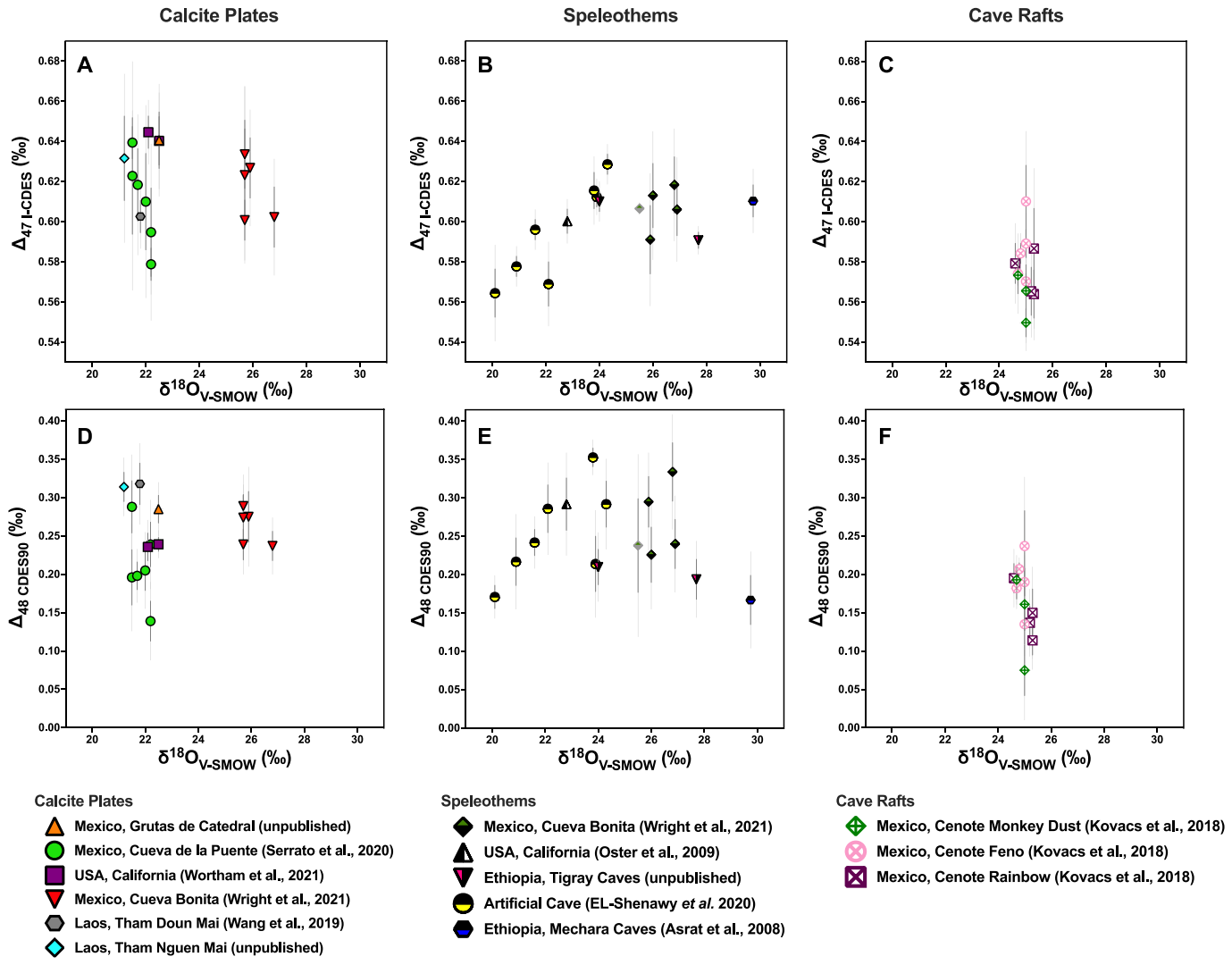

Fig. 2. Clumped isotope (Δ_{47} and Δ_{48}) versus $\delta^{18}O$ values of farmed calcite plates, speleothems (natural and synthetic), and cave rafts from multiple localities measured for this study. (A) Δ_{47} versus $\delta^{18}O$ of farmed calcite plates. (B) Δ_{47} versus $\delta^{18}O$ of speleothems. (C) Δ_{47} versus $\delta^{18}O$ of cave rafts. (D) Δ_{48} versus $\delta^{18}O$ of farmed calcite plates. (E) Δ_{48} versus $\delta^{18}O$ of speleothems. (F) Δ_{48} versus $\delta^{18}O$ of cave rafts. The speleothem sample CB4-12-Wet had only 2 replicate analyses and is indicated with an open symbol in panels B and E. Similar plots are shown with the same value ranges for direct comparison of isotopic values from the various datasets. Error bars indicate the 95 % CI (light gray) and the 68 % CI (dark gray).

by the pCO_2 gradient between the calcite-saturated water and the cave atmosphere (Dreybrodt, 2012; Hansen et al., 2013). Fast CO_2 degassing tends to result in a coherent increase (i.e., covariation) in $\delta^{18}O$ and $\delta^{13}C$ values of the dissolved bicarbonate and consequently, similar increases in the precipitating minerals due to the preferential loss of ^{12}C and ^{16}O (Mickler et al., 2004; Scholz and Hoffmann, 2008; Day and Henderson, 2011; El-Shenawy et al., 2020). At the onset of CO_2 degassing, precipitating minerals would be close to carbon and oxygen isotopic equilibrium with parent water. However, progressive CO_2 degassing leads to a positive deviation from the initial carbon and oxygen isotopic equilibria (Dreybrodt and Scholz, 2011). Therefore, a positive correlation between $\delta^{18}O$ and $\delta^{13}C$ values of cave carbonate minerals can be a robust indicator of isotopic disequilibria (Hendy, 1971; Mickler et al., 2006). The samples collected from natural caves in this study show a significant positive correlation (p-value of $\leq$0.02) between $\delta^{18}O$ and $\delta^{13}C$ values, suggesting that these samples formed in oxygen and carbon isotopic disequilibria with cave water. The calcite rafts from Mexico exhibit a $\delta^{18}O/\delta^{13}C$ covariation with a slope of 0.284 $\pm$ 0.085 (p-value = 0.008; Fig. 6A), while the farmed calcite and the natural speleothem samples from Cueva Bonita (CB) and Cueva de la Puenta (CP) caves in Mexico have slopes of 0.170 (p-value = 0.020) and 0.333 (p-value = 0.0007), respectively (Fig. 6B). This difference in the slopes of the $\delta^{18}O/\delta^{13}C$ covariation indicates a different degree of isotopic disequilibria. Note that our regression analyses were undertaken only for data sets with 3 or more samples.

The slope of $\delta^{18}O/\delta^{13}C$ covariation in carbonate minerals due to CO_2 degassing can be estimated using a Rayleigh Distillation Model (RDM) (Mickler et al., 2004, 2006; Scholz and Hoffmann, 2008; El-Shenawy et al., 2020). The estimated slopes for calcite formed under progressive CO_2 degassing in caves at 0–30 °C range between 0.919 and 1.040. The observed slopes in rafts, natural speleothems, and farmed calcite plates (0.284, 0.170 and 0.333, respectively) are significantly shallower than their estimated slopes based on RDM (0.997, 0.962 and 0.967, respectively; Fig. 6). These shallower slopes can be explained by two potential mechanisms: (1) Oxygen Isotope Exchange (OIE) between DIC species and H_2O in cave water (Beck et al., 2005; Dreybrodt and Scholz, 2011; El-Shenawy et al., 2020) and (2) Carbon Isotope Exchange (CIE) between DIC species in cave water and CO_2 in cave atmosphere (Dreybrodt et al., 2016; Hansen et al., 2017; El-Shenawy et al., 2020). Under complete or partial OIE, ^{16}O depletion (or ^{18}O enrichment) of the DIC species due to CO_2 degassing is typically buffered or minimized by the isotopic exchange with the large oxygen reservoir of cave water,

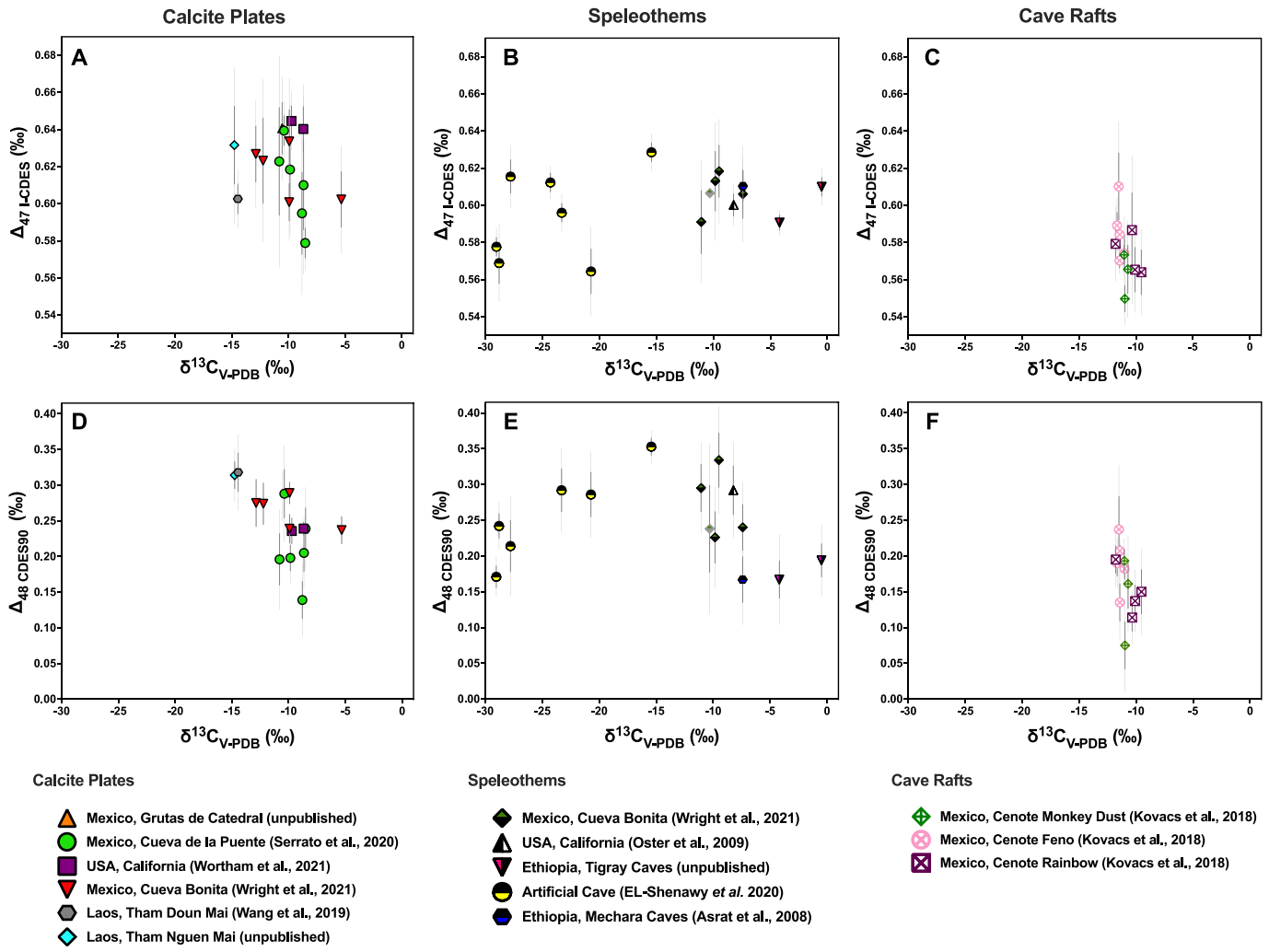

Fig. 3. Clumped (Δ_{47} and Δ_{48}) versus $\delta^{13}C$ values for farmed calcite plates, speleothems (natural and synthetic), and cave rafts measured for this study. (A) Δ_{47} versus $\delta^{13}C$ of farmed calcite plates. (B) Δ_{47} versus $\delta^{13}C$ of speleothems. (C) Δ_{47} versus $\delta^{13}C$ of cave rafts. (D) Δ_{48} versus $\delta^{13}C$ of farmed calcite plates. (E) Δ_{48} and $\delta^{13}C$ of speleothems. (F) Δ_{48} versus $\delta^{13}C$ of cave rafts. The speleothem sample CB4-12-Wet had only 2 replicate analyses and is indicated with a gray symbol in panels B and E. Similar plots are shown with the same value ranges for direct comparison of isotopic values from the various datasets. Error bars indicate the 95 % CI (light gray) and the 68 % CI (dark gray).

decreasing the slope of the $\delta^{18}O/\delta^{13}C$ covariation in precipitating minerals (Fig. 6A). Pure CO_2 degassing disequilibria is described by the RDM as a 1:1 covariation, or $\delta^{18}O/\delta^{13}C$ slope = 1 (Mickler et al., 2006). This slope is reduced with increasing contributions of OIE and CIE (Fig. 7A). When the slope = 0, the $\delta^{18}O$ values are at equilibrium.

The OIE mechanism would decrease the slope of cave carbonate minerals that grow at a slow rate (e.g., minerals formed in pools under a thick water layer) becuase oxygen isotope exchange between the DIC species and H_2O in cave water proceeds on a time scale of several hours at low temperature (Beck et al., 2005; El-Shenawy et al., 2020). In contrast, OIE is not expected to significantly contribute to the slope of fast-growing speleothems from a thin water film such as stalagmites and stalactites (Dreybrodt et al., 2016). Further, a CIE mechanism is active in a ventilated cave where cave air CO_2 is continuously replaced by atmospheric CO_2. The average $\delta^{13}C$ value of cave air CO_2 ranges from −13 ‰ to −23 ‰, which is in carbon isotope equilibrium with DIC species in cave water, whereas atmospheric CO_2 has a higher $\delta^{13}C$ value of approximately −8 ‰ (McDermott et al., 2006). As a result, when the cave air CO_2 is partially or completely replaced by atmospheric CO_2, CIE increases the $\delta^{13}C$ value of the DIC species in cave water and the precipitating carbonate minerals would have decreased $\delta^{18}O/\delta^{13}C$ covariation induced by CO_2 degassing. CIE proceeds faster than OIE (Beck et al., 2005; Dreybrodt et al., 2016; Hansen et al., 2017). El-Shenawy et al. (2020) demonstrated that a significant increase in the $\delta^{13}C$ value of stalagmite-like minerals due to CIE occurred in few hundred seconds (see their Fig. 6a). Therefore, CIE is expected to impact the CO_2 degassing slope in both fast- and slow-growing speleothems in ventilated caves.

The cave rafts from Mexico are rapidly formed at the air–water interface in three proximate caves, which are completely or partially open to the atmosphere, allowing the ventilation of cave air (Kovacs et al., 2018). The formation of rafts under these conditions suggests that the CIE mechanism is the most likely cause of the shallower slope in their $\delta^{18}O/\delta^{13}C$ covariation (Fig. 6). Likewise, speleothems and farmed calcite from Cueva Bonita grew under a seasonal ventilation mode (i.e., low pCO_2 in winter and high pCO_2 in summer; see Fig. S3A in Wright et al., 2022), allowing CIE to imprint the carbon isotope composition of the forming minerals. However, some of these samples exhibit a large spread in their $\delta^{13}C$ values with an approximately constant $\delta^{18}O$ value. The effect of OIE could be due to a relatively thicker water layer on the apex of speleothems and on the glass plate. Cueva de la Puente was described as well-ventilated and the shallower $\delta^{18}O/\delta^{13}C$ slope for its farmed calcite samples corroborates this due to the significant impact of CIE with limited to no effect of OIE. Additionally, regression analysis of

Table 3
Extent of disequilibria ($\Delta\delta^{18}O$, $\Delta\Delta_{47}$, $\Delta\Delta_{48}$) were calculated as the difference between the measured value and equilibrium value. We also compare reported and Δ_{47}-predicted temperatures. The Δ_{47}-predicted temperature was determined to agree with the measured cave temperature if the measured temperature is within the 95% CI of the predicted temperature. The Δ_{47}-predicted temperature and equilibrium clumped isotope values were determined using calibrations from Anderson et al. (2021) and Lucarelli et al. (2023a). Equilibrium $\delta^{18}O$ values were calculated using the temperature dependent relationship from Kim and O'Neil (1997) and reported $\delta^{18}O_{water}$ values (Table S1).

Sample Name	$\Delta\delta^{18}O$ (‰)	1 SE	95 % CI	$\Delta\Delta_{47}$ (‰)	1 SE	95 % CI	$\Delta\Delta_{48}$ (‰)	1 SE	95 % CI	T (°C)	Δ_{47}-T (°C)[1]	Δ_{47}-T (°C)[2]	1 SE	95 % CI	T and Δ_{47}-T agree	Δ_{47}-Δ_{48} consistent with equilibrium
B1	0.78	0.12	0.23	−0.045	0.007	0.014	−0.172	0.033	0.065	25	41	43	3	5	N	N
B3	0.59	0.02	0.05	−0.030	0.013	0.026	−0.086	0.034	0.067	25	35	36	5	10	N	N
B5	0.41	0.07	0.13	−0.022	0.005	0.009	−0.054	0.016	0.032	25	32	33	2	4	N	N
F1	0.96	0.03	0.06	−0.026	0.004	0.007	−0.112	0.026	0.051	24	33	34	1	3	N	N
F2	−0.91	0.02	0.04	0.014	0.018	0.035	−0.010	0.046	0.090	24	20	20	6	11	Y	**Y**
F3	0.84	0.05	0.09	−0.007	0.007	0.015	−0.057	0.018	0.035	24	27	27	3	5	Y	N
F4	−0.91	0.11	0.22	−0.022	0.010	0.020	−0.065	0.014	0.027	24	32	33	4	7	N	N
F5	0.04	0.10	0.20	−0.012	0.005	0.010	−0.040	0.008	0.015	24	28	29	2	4	Y	N
R1	1.20	0.05	0.09	−0.009	0.020	0.040	−0.132	0.019	0.038	25	27	28	7	14	Y	N
R2	0.50	0.02	0.04	−0.016	0.010	0.020	−0.052	0.019	0.038	25	30	31	4	7	Y	N
R3	1.03	0.09	0.17	−0.031	0.012	0.023	−0.096	0.031	0.060	25	36	37	4	9	N	N
R5	N/A	0.08	0.16	−0.030	0.012	0.023	−0.109	0.022	0.044	25	35	36	4	9	N	N
CB-D6	0.13	0.04	0.08	0.019	0.017	0.034	0.035	0.015	0.028	18	12	12	5	10	Y	**Y**
CB-D62	0.14	0.02	0.04	−0.013	0.010	0.020	−0.015	0.020	0.039	18	23	23	4	7	Y	**Y**
CB3	1.25	0.03	0.05	−0.011	0.015	0.029	−0.017	0.019	0.037	18	22	22	5	10	Y	**Y**
CB4-Scar	0.46	0.03	0.05	0.014	0.015	0.029	0.021	0.033	0.065	19	14	14	5	9	Y	**Y**
CB4-Scar2	0.19	0.05	0.09	0.010	0.023	0.044	0.020	0.029	0.056	18	16	15	7	13	Y	**Y**
CB4-12-Wet	−0.04	0.00	0.01	−0.007	0.002	0.003	−0.017	0.061	0.119	18	21	21	1	1	N	N
CB4-48-Dry	1.22	0.02	0.05	0.005	0.014	0.028	0.080	0.038	0.075	18	17	17	5	9	Y	**Y**
CB4-82-Wet	0.43	0.04	0.07	0.000	0.016	0.032	−0.028	0.036	0.071	18	19	19	5	10	Y	**Y**
CB4-99-Dry	1.34	0.07	0.13	−0.007	0.013	0.026	−0.014	0.032	0.063	18	21	21	4	9	Y	**Y**
CB4-Top	0.29	0.02	0.03	−0.022	0.017	0.033	0.041	0.033	0.064	18	26	27	6	11	Y	**Y**
CP-D2	−0.25	0.04	0.09	0.008	0.029	0.057	−0.059	0.036	0.070	18	16	15	8	16	Y	**Y**
CP-D3a	0.74	0.11	0.21	−0.017	0.022	0.044	−0.115	0.026	0.051	19	25	25	8	15	Y	N
CP-D3a2	0.78	0.07	0.14	0.001	0.024	0.048	−0.047	0.026	0.050	20	20	20	8	15	Y	**Y**
CP-D3a3	0.41	0.09	0.17	0.032	0.008	0.016	0.037	0.034	0.068	20	11	10	2	5	N	**Y**
CP-D3b	0.79	0.04	0.08	−0.033	0.008	0.015	−0.014	0.029	0.058	19	30	31	3	6	N	N
CP-D3b2	0.39	0.10	0.20	0.009	0.018	0.035	−0.054	0.018	0.035	20	17	17	6	11	Y	N
GC	0.54	0.09	0.17	0.015	0.014	0.028	0.025	0.018	0.035	14	10	10	4	8	Y	**Y**
TM-D10	0.45	0.04	0.09	0.000	0.008	0.016	0.069	0.027	0.053	22	22	22	3	5	Y	N
TNM	−0.07	0.06	0.11	0.031	0.021	0.042	0.065	0.019	0.038	23	13	13	6	12	Y	N
CPY	1.29	0.02	0.04	−0.002	0.008	0.016	−0.003	0.018	0.035	7	9	9	2	5	Y	**Y**
GLR	1.68	0.03	0.06	−0.006	0.012	0.024	−0.068	0.009	0.018	7	10	10	4	7	Y	N
Moaning Cave	−0.09	0.02	0.05	−0.016	0.006	0.011	0.037	0.034	0.067	18	23	23	2	4	N	N
MIE-15-95-9-FL-Center	0.45	0.01	0.01	−0.011	0.005	0.009	−0.045	0.036	0.070	15	19	19	2	3	N	N
MIE-15-95-9-FU-Edge	1.06	0.02	0.05	−0.008	0.009	0.017	0.095	0.012	0.023	15	18	18	3	6	Y	N
MIE-15-95-9-SL-Center	−0.06	0.01	0.02	0.005	0.005	0.010	0.034	0.030	0.059	15	14	14	2	3	Y	**Y**
MIE-25-95-8-FL-Center	0.44	0.01	0.02	0.002	0.005	0.010	−0.004	0.017	0.034	25	24	25	2	4	Y	**Y**
MIE-25-95-8-FU-Edge	1.44	0.02	0.04	−0.025	0.011	0.021	0.040	0.031	0.060	25	34	35	4	8	N	N
MIE-32-95-3-FL-Center	0.22	0.01	0.02	−0.010	0.012	0.024	−0.067	0.015	0.028	32	36	37	5	9	Y	N
MIE-32-95-3-FU-Center	1.77	0.02	0.04	0.003	0.005	0.010	−0.021	0.031	0.062	32	31	31	2	4	Y	**Y**
ASFA	1.30	0.02	0.03	−0.004	0.008	0.016	−0.088	0.032	0.063	18	20	20	3	5	Y	N
MM1	N/A	0.02	0.03	−0.008	0.004	0.007	−0.054	0.026	0.050	24	26	27	1	3	Y	**Y**
ZA-3	N/A	0.01	0.03	0.012	0.005	0.010	−0.037	0.023	0.045	24	20	20	2	3	N	N

[1] Anderson et al. (2021).
[2] Lucarelli et al. (2023a).

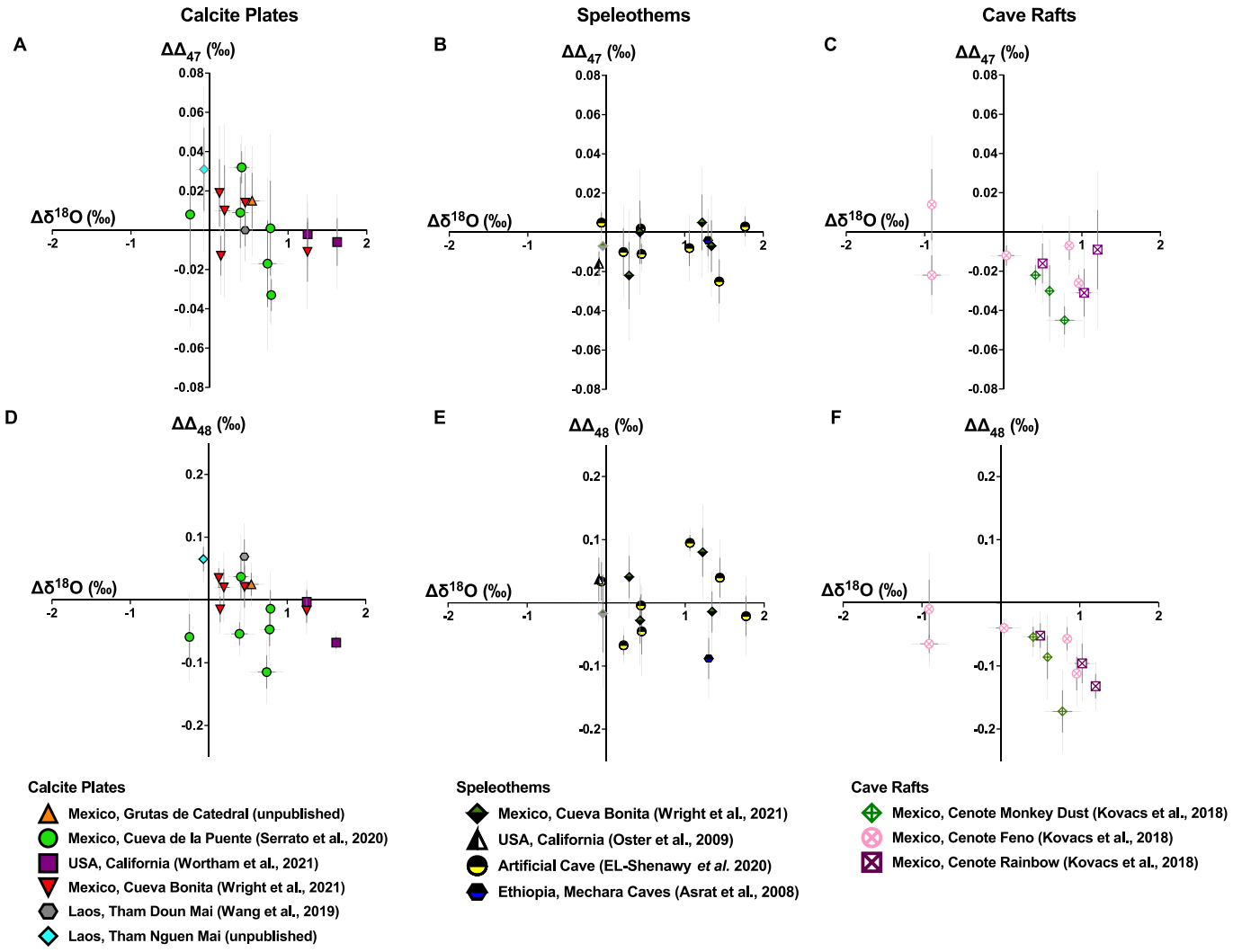

Fig. 4. Extent of disequilibria in Δ_{47}, Δ_{48}, and $\delta^{18}O$ values. $\Delta\Delta_{47}$, $\Delta\Delta_{48}$, and $\Delta\delta^{18}O$ values were calculated as the difference between measured sample values and equilibrium values for clumped (Lucarelli et al., 2023a) and oxygen isotopes (Kim and O'Neil, 1997) based on independently determined cave temperatures and $\delta^{18}O_{water}$ values. (A) $\Delta\Delta_{47}$ versus $\Delta\delta^{18}O$ of farmed calcite plates. (B) $\Delta\Delta_{47}$ versus $\Delta\delta^{18}O$ of speleothems. (C) $\Delta\Delta_{47}$ versus $\Delta\delta^{18}O$ of cave rafts. (D) $\Delta\Delta_{48}$ versus $\Delta\delta^{18}O$ of farmed calcite plates. (E) $\Delta\Delta_{48}$ versus $\Delta\delta^{18}O$ of speleothems. (F) $\Delta\Delta_{48}$ versus $\Delta\delta^{18}O$ of cave rafts. The speleothem sample CB4-12-Wet had only 2 replicate analyses and is indicated with a gray symbol in panels B and E. Error bars indicate the 95 % CI (light gray) and the 68 % CI (dark gray).

the artificial speleothem samples from the McMaster artificial cave was not possible due to the limited number of samples from each experimental condition (only one or two samples). However, the samples from the upper watch glasses (FU samples) were shown to be affected by CIE, whereas the lower watch glass samples were controlled by both the CIE and the OIE (El-Shenawy et al., 2020). In summary, oxygen and carbon isotope exchange between cave atmosphere/water and DIC species are key controls on isotopic values, in combination with CO_2 degassing during carbonate mineral precipitation in cave environments. The contributions from these processes to measured isotopic values is difficult to disentangle using $\delta^{18}O/\delta^{13}C$ covariation alone.

5.2. *Examining clumped isotope disequilibrium in caves using modeled and measured values*

By pairing Δ_{48} and Δ_{47} values, we can predict and model different disequilibria processes (Guo, 2020; Bajnai et al., 2021, Parvez et al., 2023; Lucarelli et al., 2023b). This can augment traditional degassing disequilibria probing techniques, such as linear regression using RDM (Figs. 6, 7). Dual clumped isotopes have been used to correct disequilibria-induced temperature biases (Bajnai et al., 2021) through trajectory predictions using the IsoDIC model (Guo, 2020), which is a major advancement in our understanding of dual clumped isotope disequilibria. However, universal application of this approach is somewhat limited due to the complex nature of cave carbonate formation which the IsoDIC model does not fully encompass (Guo, 2020). In the CO_2 degassing and CO_2 absorption regime, IsoDIC focuses on speleothem, biogenic carbonates (i.e., corals), and high-pH travertines. However, it is acknowledged to oversimplify speleothem formation and coral calcification processes (Guo, 2020).

Fig. 7B is a generic schematic of absorption and degassing processes in $\Delta\Delta_{47}$-$\Delta\Delta_{48}$ space. CO_2 degassing disequilibrium is predicted to originate in quadrant 2 and evolve through quadrant 1 as oxygen isotopes exchange. A similar cycle occurs for CO_2 absorption disequilibrium as $\Delta\Delta_{47}$-$\Delta\Delta_{48}$ values evolve from quadrant 4 to quadrant 3. The slopes determined from the origin to the initial departure from equilibrium in both CO_2 absorption and degassing disequilibria were used by Bajnai et al. (2020) to correct clumped isotope temperature predictions of warm- and cold-water coral (absorption) along with natural and synthetic speleothems (degassing). However, we hypothesize this very simplified correction may become far more difficult to make when cave carbonates have additional isotopic buffering effects that displace them

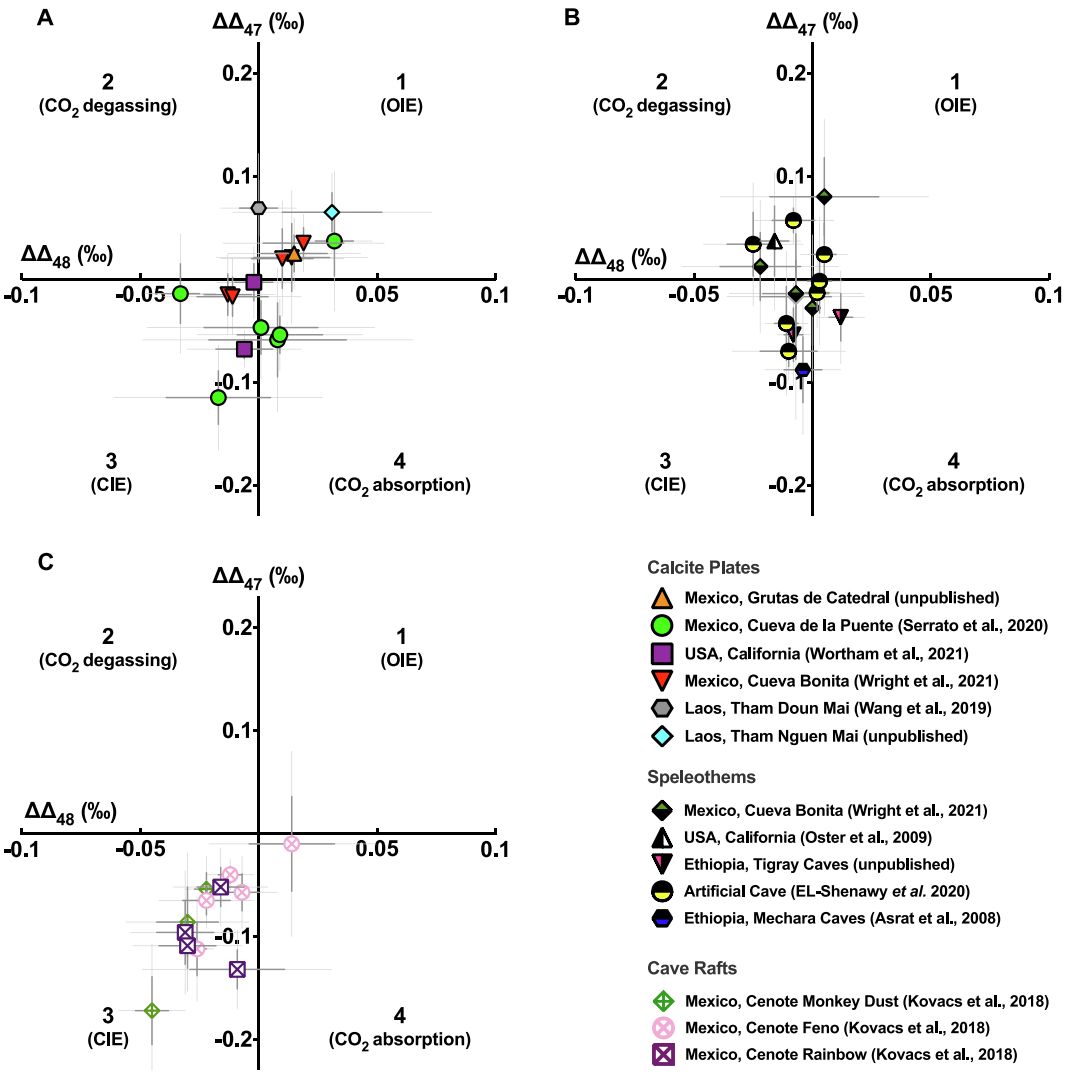

Fig. 5. Extent of disequilibria in sample Δ_{47} and Δ_{48} values for farmed calcite plates, speleothems, and cave rafts. $\Delta\Delta_{47}$ and $\Delta\Delta_{48}$ values were calculated as the difference between measured sample values and calculated equilibrium (Lucarelli et al., 2023a) for each sample based on independent constraints on cave temperatures. Each quadrant is labelled with the dominant mechanism of disequilibria determined from IsoDIC model (Guo, 2020) calculations. (A) $\Delta\Delta_{47}$ versus $\Delta\Delta_{48}$ for farmed calcite plates. (B) $\Delta\Delta_{47}$ versus $\Delta\Delta_{48}$ for speleothems. C) $\Delta\Delta_{47}$ versus $\Delta\Delta_{48}$ for cave rafts. The linear regression slope for all cave raft samples, which may be biased by CIE, is 2.181 ± 0.632. The speleothem sample CB4-12-Wet had only 2 replicate analyses and is indicated with a gray symbol in panel B. Error bars indicate the 95 % CI (light gray) and the 68 % CI (dark gray).

from the initial disequilibrium slopes.

In caves, oxygen and carbon isotope exchange can result in alterations to the isotopic composition of the DIC pool which can affect both Δ_{47} and Δ_{48} signatures. OIE is a homogenous process and based primarily on (de)hydration and (de)hydroxylation (reactions (6) and (7)). Homogenous (same phase) OIE between DIC and H_2O reservoirs within cave water can result in isotopic buffering of the ^{18}O enrichment in the DIC pool induced by CO_2 degassing (Beck et al., 2005; Mickler et al., 2006; Dreybrodt and Scholz, 2011), resulting in migrations from the traditional degassing pathway. In contrast, CIE is a heterogenous reaction, where carbon isotope exchange occurs between DIC in cave water and CO_2 in cave atmosphere. Heterogeneous CIE between two phases has been far less studied than OIE, and may result in Δ_{47} and Δ_{48} disequilibrium effects that are inconsistent with CO_2 degassing. Previous research suggests that well-ventilated caves will exhibit greater amounts of CIE (Dreybrodt and Scholz, 2011; Dreybrodt et al., 2016; Hansen et al., 2017; El-Shenawy et al., 2020).

Disequilibria associated with cave rafts from Mexico recovered by Kovacs et al. (2018) exhibit depletions in both Δ_{47} and Δ_{48}, consistent with effects from CIE (Fig. 5C). The relatively deep water (for example, compared to a thin film) of the Mexican cave pools would promote greater residence times of DIC in the system, resulting in OIE and CIE, corroborating the shallow $\delta^{18}O/\delta^{13}O$ slopes (Figs. 6A, 7A). In addition, the extent of CIE effects on Δ_{47} and Δ_{48} values of the cave rafts appears to be a function of ventilation. Cenote Feno is considered to have the least ventilation of the three Cenotes, with a small opening to atmosphere. Cenotes Rainbow and Monkey Dust were considered well-ventilated with large openings to the atmosphere (Kovacs et al., 2018). Previous research indicates this effect is enhanced in well-ventilated caves (Dreybrodt et al., 2016; Hansen et al., 2017; El-Shenawy et al., 2020). This is consistent with samples collected from Monkey Dust (B1, B3, B5) and Rainbow (R1, R2, R3, R5), which had large and comparable departures from the equilibrium (origin in Fig. 5) to the average $\Delta\Delta_{47}$ and $\Delta\Delta_{48}$ values ($\overline{\Delta\Delta_{47}}$, $\overline{\Delta\Delta_{48}}$) for each cave (Monkey Dust: $\overline{\Delta\Delta_{47}} = -0.032 \pm 0.007$ ‰, $\overline{\Delta\Delta_{48}} = -0.104 \pm 0.035$ ‰; Rainbow: $\overline{\Delta\Delta_{47}} = -0.021 \pm 0.006$ ‰, $\overline{\Delta\Delta_{48}} = -0.097 \pm 0.017$ ‰), corroborating a well-ventilated cave. Samples from Cenote Feno (F1, F2, F3, F4, F5) had the smallest departure into quadrant 3 ($\overline{\Delta\Delta_{47}} = -0.011$

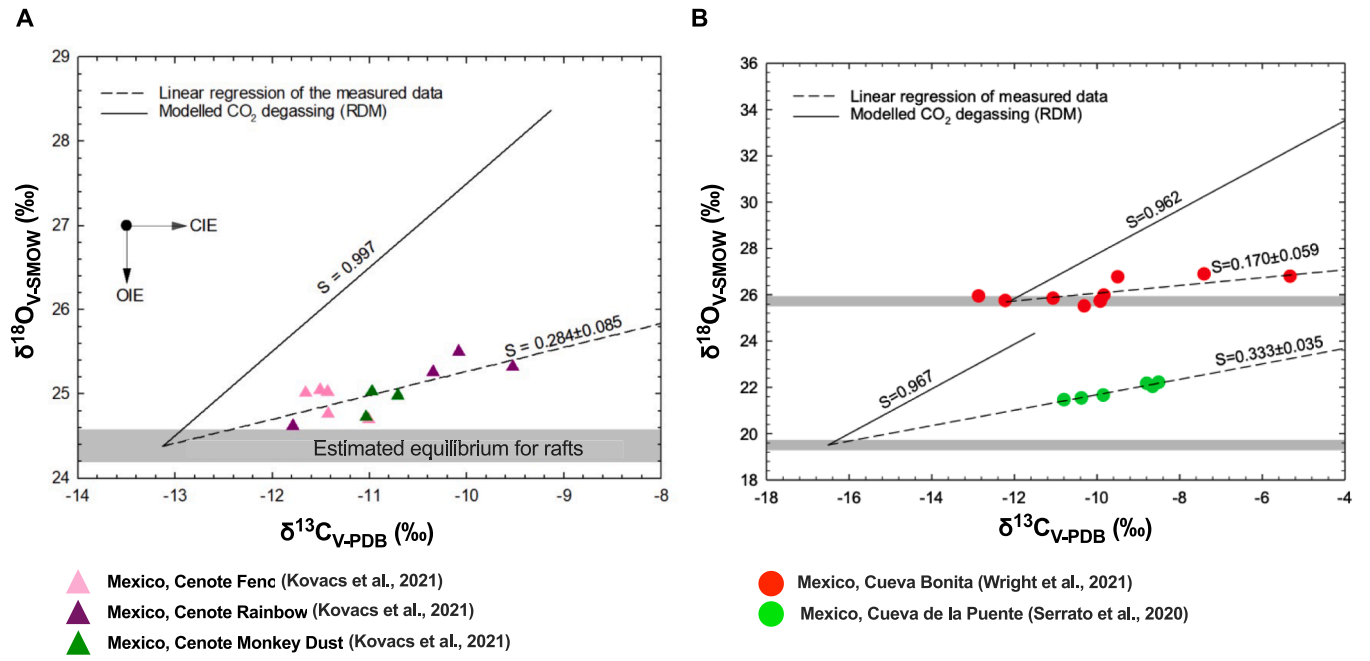

Fig. 6. Disequilibria slopes for $\delta^{18}O$ versus $\delta^{13}C$ of cave rafts (Kovacs et al., 2018; triangles), natural speleothems (Wright et al., 2022; red circles), and farmed speleothems (Serrato, 2020; green circles) from Mexico. The cave raft samples were aggregately assessed and not separated based on individual cenotes. The linear regression (dashed lines) slopes are 0.284 ± 0.085 for cave rafts, 0.170 ± 0.059 for Cueva Bonita speleothems, and 0.333 ± 0.035 for Cueva de la Puente speleothems. The measured slopes are significantly shallower than RDM predicted slopes (solid lines) of 0.997 for cave rafts, 0.962 for Cueva Bonita speleothems, and 0.967 for Cueva de la Puenta speleothems. Error bars are smaller than the symbols.

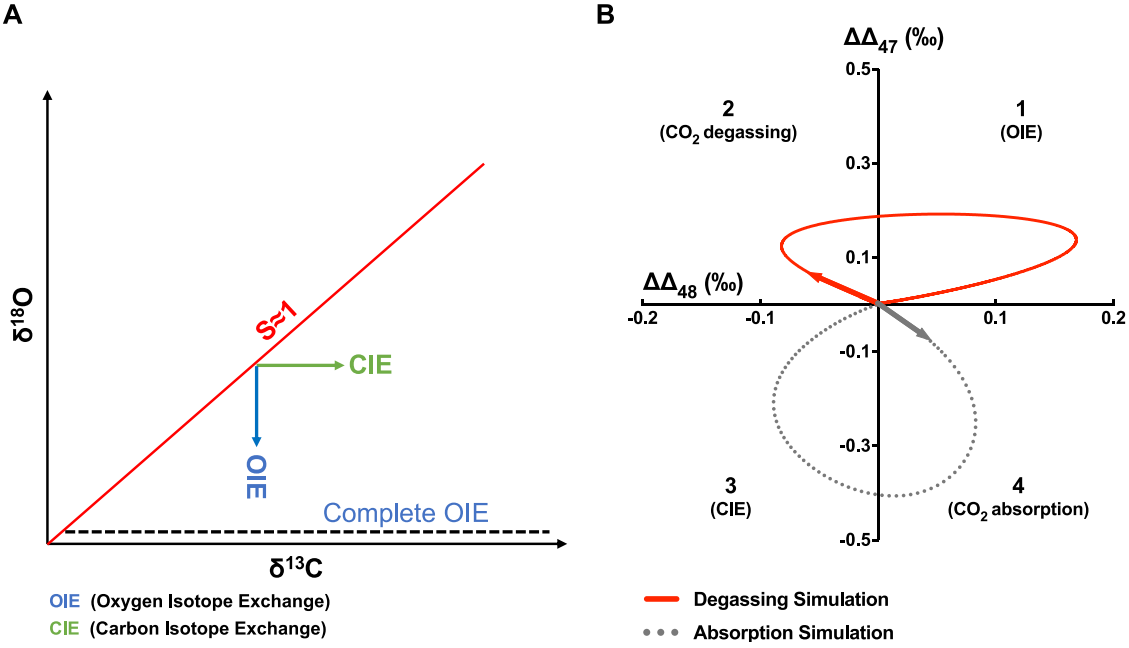

Fig. 7. Modeled bulk stable isotope ($\delta^{18}O$, $\delta^{13}C$) and clumped isotope ($\Delta\Delta_{47}$, $\Delta\Delta_{48}$) disequilibria. (A) CO_2 degassing disequilibria using a Rayleigh Distillation Model (RDM). A slope value (S) of 1 simulates pure CO_2 degassing disequilibria. Oxygen Isotope Exchange (OIE; blue line) and Carbon Isotope Exchange (CIE; green line) shift the slope to $S < 1$. Complete OIE (black dashed line) results in a $S = 0$, where the $\delta^{18}O$ values are at isotopic equilibrium. (B) Disequilibria evolution of $\Delta\Delta_{47}$ and $\Delta\Delta_{48}$ from CO_2 degassing (red curve) and CO_2 absorption (gray dotted curve). Quadrants 1 through 4 indicate the dominant mechanism of disequilibrium that we hypothesize would result in $\Delta\Delta_{47}$ and $\Delta\Delta_{48}$ values in the respective quadrants. CO_2 absorption (grey arrow) and degassing (red arrow) vectors were calculated with the IsoDIC (Guo et al., 2019; Guo, 2020) model using default parameters.

± 0.007 ‰, $\overline{\Delta\Delta_{48}} = -0.057 \pm 0.017$ ‰), corroborating a poorly ventilated cave system relative to the other Cenotes.

Farmed calcite plates and speleothems recovered from Cueva Bonita (Wright et al., 2022) were largely indistinguishable from equilibrium values, with the majority of samples within error of equilibrium (Fig. 5A). The Δ_{47}-temperature values determined with these samples are consistent with reported temperatures (Table 3). Farmed calcite

plates recovered from Cueva de la Puente (Serrato, 2020) are consistent with CIE occurring during CO_2 absorption, which is consistent with the $\delta^{18}O/\delta^{13}C$ slope of 0.333 ± 0.035 (Fig. 6B).

While $\delta^{18}O/\delta^{13}C$ regression analysis could not resolve CIE or OIE in the synthetic speleothems (El-Shenawy et al., 2020), we can attempt to test for this with $\Delta\Delta_{47}$ and $\Delta\Delta_{48}$ values. The sample set from an artificial cave (El-Shenawy et al., 2020) has relatively even distribution with biases in quadrant 2 (CO_2 degassing) and quadrant 3 (CIE) (Fig. 5B). Samples MIE-25-95-8-FU-Edge and MIE-15-95-9-FU-Edge had the greatest CO_2 degassing effects (Table 3) and were collected from the upper glasses where the convex nature of the glass plate prevented pooling of the drip water. This is consistent with what we would expect to see with natural speleothems and associated CO_2 degassing phenomenon (Fiebig et al., 2019; Guo and Zhou, 2019; Guo, 2020; Bajnai et al., 2020). However, samples MIE-15-95-9-FL-Center and MIE-32-95-3-FL-Center fall within quadrant 3, which indicates KIE associated with CIE are present. This confirms what El-Shenawy et al. (2020) reported for their samples collected from the lower watch glass indicating CIE and OIE. We only observed CIE in our dataset because we analyzed a limited sample set from their study. This was also consistent with speleothem samples from Mexico, the U.S., and Ethiopia (Fig. 5B).

Dual clumped isotopes can be used to examine individual samples. The sample GLR collected from Lilburn Cave (Wortham et al., 2021) exhibited CIE, residing in quadrant 3 of Fig. 5A. This farmed calcite plate was collected from a drip site located near the cave entrance with seasonal ventilation variations. Sample TM-D10 collected from Tham Doun Mai (Wang et al., 2019) resides directly in between quadrant 1 and 2, indicating potential contributions to isotopic values from degassing and OIE in a closed cave system (Fig. 5A). This can be due to increased thickness of water film and pooling of water due to significant rainfall (1200 mm) localized during the summer (June–September) monsoon season (Wang et al., 2019). This accounts for what we see with sample TNM collected from Tham Nguen Mai (unpublished), a proximate location to Tham Doun Mai. This sample is a part of unpublished work, so site information is limited, however, it resides in quadrant 1 (Fig. 5A), similar to sample TM-D10, indicating OIE effects driving it back to equilibrium. The speleothem sample Moaning Cave (Oster et al., 2009) falls within quadrant 2, similar to samples CPY and GLR from Lilburn cave, which are in the same region. Although cave ventilation information was not provided for this sample, we can infer that there is ventilation which is driving CIE. The samples collected from Mechara (Asrat et al., 2008) and Tigray (unpublished) caves on the Ethiopian highlands have similar biases from CIE. Sample MM1 recovered from Mai Mekden cave was collected from a ledge proximate to the cave entrance which provided good exposure to outside atmospheric CO_2, while ZA-3 was collected from a well-ventiliated wide, horizontal chamber about 20 m from the entrance of the Zayei cave. Sample ASFA collected from Mechara cave is located within 25 m of the cave entrance in a vertical orientation. The Asfa chamber of the cave is well ventilated, and based on the data presented in Fig. 5B, we infer that the ventilation was sufficient to promote CIE.

5.3. Potential temperature reconstruction using cave carbonates

One of the most promising applications of the dual clumped isotope method is its ability to test dis/equilibrium isotope conditions in fossil speleothems and therefore, their potential as a terrestrial paleoclimate archive. Measurements of Δ_{47}-Δ_{48} have a characteristic equilibrium relationship that does not depend on the drip water isotopic composition. We can use this tool to identify samples at isotopic equilibrium and then determine paleotemperatures using a Δ_{47}-temperature calibration, or other methods for palaeothermometry based on oxygen isotopes (such as fluid inclusion-carbonate mineral thermometry).

Here, 19 of 44 samples had Δ_{47}-Δ_{48} values that were indistinguishable from equilibrium. Of these 19 quasi-equilibrium samples, 18 (95 %) yielded Δ_{47} values that accurately predicted the independently reported formation temperature when utilizing a published calibration (Fig. 8; Table 3). This is in stark contrast to the 25 samples that did not have Δ_{47}-Δ_{48} values consistent with equilibrium, where only 12 (48 %) accurately predicted the reported formation temperature (Fig. 8; Table 3). This supports prior findings that if samples have equilibrium dual clumped isotope values, they can be used to accurately reconstruct temperatures (Fiebig et al., 2019, 2021; Guo, 2020; Bajnai et al., 2020; Lucarelli et al., 2023a).

6. Conclusion

We have conducted dual clumped (Δ_{47}, Δ_{48}) and traditional stable ($\delta^{18}O$, $\delta^{13}C$) isotope analysis of 44 modern cave carbonate mineral samples, including natural and artificial speleothems, farmed calcite plates, and cave rafts from 13 caves and cenotes. To determine dominant disequilibria mechanisms, we used linear regressions of different isotopic measurements including $\delta^{18}O/\delta^{13}C$ slopes, Rayleigh Distillation Modeling, and dual clumped isotope analysis. Overall, 19 samples formed in equilibrium based on Δ_{47}-Δ_{48} measurements, and 18 of these equilibrium samples accurately predicted reported cave temperatures. In contrast, 25 The samples had disequilibrium Δ_{47}-Δ_{48} values, and the majority failed to accurately predict reported cave temperatures. These findings suggest that dual clumped isotopes can be used to identify cave carbonate minerals that formed under equilibrium conditions, thus, may yield accurate Δ_{47}-based terrestrial temperature reconstructions. We suggest speleothems, specifically, would be a target for paleoclimate reconstructions, as 44 % of speleothem samples achieved Δ_{47}-Δ_{48} equilibrium.

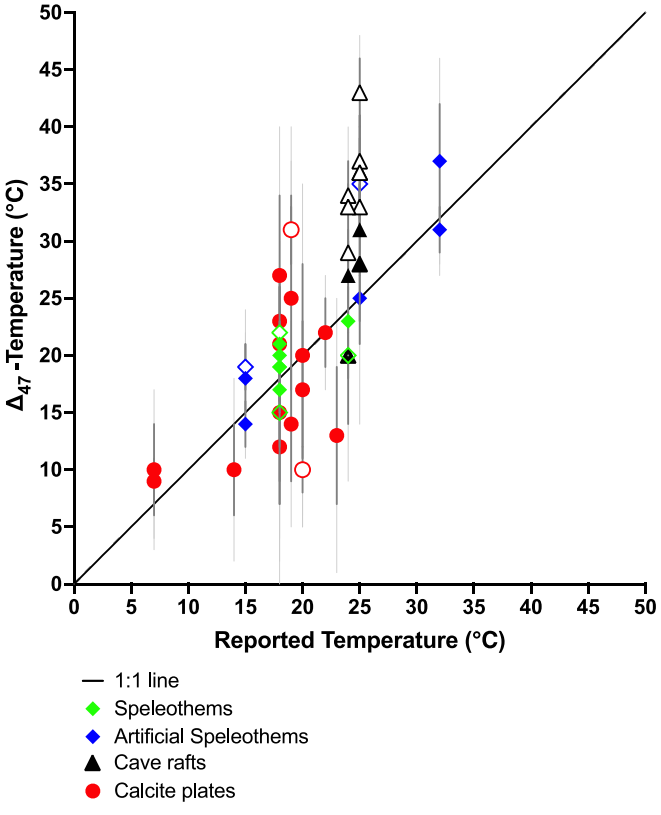

Fig. 8. Comparison of Δ_{47}-temperatures determined for all cave carbonate mineral samples analysed here versus reported cave temperatures. Overall, 19 out of 44 samples have reported temperatures within the 95 % CI of the Δ_{47}-temperatures (filled symbols). The 25 samples with Δ_{47}-temperatures that do not accurately reflect formation temperature have open symbols, where 21 samples are biased by Δ_{47} values that are depleted relative to equilibrium. Error bars indicate the 95 % CI (light gray) and the 68 % CI (dark gray).

Some of the samples examined here have disequilibrium clumped isotope values which are not explained by CO_2 degassing. We suggest that samples that exhibit enrichment in both Δ_{47} and Δ_{48} values relative to equilibrium (i.e., fall within quadrant 1 of our schematic of $\Delta\Delta_{47}$-$\Delta\Delta_{48}$) are indicative of cases where there is homogenous oxygen isotope exchange between DIC and H_2O in cave water that can occur with longer residence time due to various conditions, such as water layer thickness. We hypothesize cave carbonate minerals may exhibit depletion in both Δ_{47} and Δ_{48} relative to equilibrium (i.e., fall within quadrant 3 of the $\Delta\Delta_{47}$-$\Delta\Delta_{48}$ space of our schematic) because of heterogeneous carbon isotope exchange between DIC in cave water and CO_2 in cave atmosphere. This hypothesis is supported by Rayleigh Distillation Modeling of traditional stable isotopes, and knowledge of cave conditions (i.e., increased ventilation) that indicate conditions conducive to isotope disequilibria. Cave rafts examined here exhibit evidence for strong CIE as indicated by a flattened slope in the Rayleigh Distillation Modeling linear regression analysis and relatively large depletions in Δ_{47} and Δ_{48} when compared to speleothems or farmed calcite plates. The extent of Δ_{47} and Δ_{48} disequilibrium has a correlation to relative cave ventilation. Most farmed calcite plates and speleothems examined in this study exhibit some degree of kinetic isotope effects associated with oxygen isotope exchange or carbon isotope exchange, with a minority exhibiting dominant CO_2 degassing effects as indicated by Rayleigh Distillation Modeling, linear regression analysis, and deviations from Δ_{47}-Δ_{48} equilibrium. Many of the samples analyzed in this study that exhibit disequilibrium Δ_{47}-Δ_{48} values due to oxygen and carbon isotope exchange are not explained through existing models for cave carbonates which only account for isotopic effects from CO_2 degassing, and represents an area for future work.

Declaration of competing interest

The authors declare that they have no known competing financial interests or personal relationships that could have appeared to influence the work reported in this paper.

Acknowledgments

We thank lab members past and present for their work running standards, efforts in data entry, and contributions to discussions. We also thank David Richards and an anonymous reviewer for their helpful comments. This work was funded by DOE BES grant DE-FG02-83613ER16402 and Heising-Simons Foundation grant 2022-3314 to Aradhna Tripati and Natural Science and Engineering Research Council (NSERC) Discovery Grants Program (386188-2010, 2015-04413, & 2020-05810) to Sang-Tae Kim. Zeeshan Parvez, Irvin Matamoros, Joshua Rubi, Kevin Miguel, Randy Flores, Jamie Lucarelli, and Robert Ulrich also acknowledge support from fellowships granted by The Center for Diverse Leadership in Science supported by the Packard Foundation, Sloan Foundation, Silicon Valley Community Foundation, and NSF (ICER-2039462 and RISE-2232606). Zeeshan Parvez received support as a Tillman and Sentinels of Freedom Scholar. Jamie Lucarelli received support from Cota Robles and Dissertation Year Fellowships from the University of California, Los Angeles and by an Institutional Research and Academic Career Development Award (IRACDA; 5K12GM106996). Daniel Gebregiorgis acknowledges support from NSF grant 2002509. Asfawoseen Asrat acknowledges support from START-PACOM. We thank Ben Elliot and members of the Eagle-Tripati lab for their technical support in mass spectrometry. Kathleen Johnson acknowledges support from the National Science Foundation (awards 1405472, 1603056, 1806090, and 2103129). Kathleen Johnson and Kevin Wright acknowledge Jean-Louis Lacaille-Muzquiz, Esteban Berrones, Gabriela Serrato-Marks, and Sergio Sanchez-Armass for assistance with cave monitoring and fieldwork in Cueva de la Puente and Cueva Bonita. Kathleen Johnson acknowledges Norseng Sayvongdouane, Sengphone Keophanhya, Terry Bolger, Andrea Borsato, and Silvia Frisia for assistance with fieldwork in Tham Doun Mai and Tham Ngeun Ma. Author Contributions: AT initiated and supported the work and supervised the students and postdoctoral researchers at UCLA and East LA College, with analyses conducted in her laboratory. AT and STK designed the research. ZP, ME, and JL coauthored the manuscript with guidance from AT, RE, STK and input from all coauthors. ME, ER, DG, AA, IM, and KJ provided samples. ZP, JK, IM, JR, KM, BE, RF performed the isotope analyses and calculations with input from AT. All authors contributed insights to data analyses and interpretations and edited the manuscript.

Data availability

Research data has been supplied via a repository: https://doi.org/10.5281/zenodo.10161309.

Appendix A. Supplementary material

Supplementary material contains additional figures, including a map of Cenote Rainbow, Feno, and Monkey Dust, Mexico Cave Samples, and cross plots of stable isotope data. Model equations, $\delta^{18}O_{water}$ values for each sample, standard mean values, and reproducibility of standard Δ_{47}, Δ_{48}, $\delta^{18}O$, and $\delta^{13}O$ are reported. Supplementary material to this article can be found online at https://doi.org/10.1016/j.gca.2023.11.017.

References

Affek, H.P., Bar-Matthews, M., Ayalon, A., Matthews, A., Eiler, J.M., 2008. Glacial/interglacial temperature variations in Soreq cave speleothems as recorded by 'clumped isotope' thermometry. Geochim. Cosmochim. Acta 72, 5351–5360.

Affek, H.P., Zaarur, S., 2014. Kinetic isotope effect in CO_2 degassing: Insight from clumped and oxygen isotopes in laboratory precipitation experiments. Geochim. Cosmochim. Acta 143, 319–330.

Affolter, S., Fleitmann, D., Leuenberger, M., 2014. New online method for water isotope analysis of speleothem fluid inclusions using laser absorption spectroscopy (WS-CRDS). Clim. Past 10, 1291–1304.

Almogi-Labin, A., Bar-Matthews, M., Shriki, D., Kolosovsky, E., Paterne, M., Schilman, B., Ayalon, A., Aizenshtat, Z., Matthews, A., 2009. Climatic variability during the last ~90ka of the southern and northern Levantine Basin as evident from marine records and speleothems. Quat. Sci. Rev. 28, 2882–2896.

Anderson, N.T., Kelson, J.R., Kele, S., Daëron, M., Bonifacie, M., Horita, J., Mackey, T.J., John, C.M., Kluge, T., Petschnig, P., Jost, A.B., Huntington, K.W., Bernasconi, S.M., Bergmann, K.D., 2021. A unified clumped isotope thermometer calibration (0.5–1,100°C) using carbonate-based standardization. Geophys. Res. Lett. 48.

Asrat, A., Baker, A., Leng, M., 2008. Environmental monitoring in the Mechara caves, Southeastern Ethiopia: implications for speleothem palaeoclimate studies. KIP Artic.

Bajnai, D., Fiebig, J., Tomašových, A., Milner, G.S., Rollion-Bard, C., Raddatz, J., Löffler, N., Primo-Ramos, C., Brand, U., 2018. Assessing kinetic fractionation in brachiopod calcite using clumped isotopes. Sci. Rep. 8, 533.

Bajnai, D., Guo, W., Spötl, C., Coplen, T.B., Methner, K., Löffler, N., Krsnik, E., Gischler, E., Hansen, M., Henkel, D., Price, G.D., Raddatz, J., Scholz, D., Fiebig, J., 2020. Dual clumped isotope thermometry resolves kinetic biases in carbonate formation temperatures. Nat. Commun. 11, 4005.

Bajnai, D., Coplen, T.B., Methner, K., Löffler, N., Krsnik, E., Fiebig, J., 2021. Devils hole calcite was precipitated at ±1°C stable aquifer temperatures during the last half million years. Geophys. Res. Lett. 48.

Bar-Matthews, M., Ayalon, A., Kaufman, A., 1997. Late Quaternary Paleoclimate in the Eastern Mediterranean Region from Stable Isotope Analysis of Speleothems at Soreq Cave, Israel. Quat. Res. 47, 155–168.

Bar-Matthews, M., Ayalon, A., Gilmour, M., Matthews, A., Hawkesworth, C.J., 2003. Sea–land oxygen isotopic relationships from planktonic foraminifera and speleothems in the Eastern Mediterranean region and their implication for paleorainfall during interglacial intervals. Geochim. Cosmochim. Acta 67, 3181–3199.

Beck, W.C., Grossman, E.L., Morse, J.W., 2005. Experimental studies of oxygen isotope fractionation in the carbonic acid system at 15°, 25°, and 40°C. Geochim. Cosmochim. Acta 69, 3493–3503.

Bernasconi, S.M., Daëron, M., Bergmann, K.D., Bonifacie, M., Meckler, A.N., Affek, H.P., Anderson, N., Bajnai, D., Barkan, E., Beverly, E., Blamart, D., Burgener, L., Calmels, D., Chaduteau, C., Clog, M., Davidheiser-Kroll, B., Davies, A., Dux, F., Eiler, J., Elliott, B., Fetrow, A.C., Fiebig, J., Goldberg, S., Hermoso, M., Huntington, K.W., Hyland, E., Ingalls, M., Jaggi, M., John, C.M., Jost, A.B., Katz, S., Kelson, J., Kluge, T., Kocken, I.J., Laskar, A., Leutert, T.J., Liang, D., Lucarelli, J., Mackey, T.J., Mangenot, X., Meinicke, N., Modestou, S.E., Müller, I.A., Murray, S., Neary, A., Packard, N., Passey, B.H., Pelletier, E., Petersen, S., Piasecki, A., Schauer, A., Snell, K.E., Swart, P.K., Tripati, A., Upadhyay, D., Vennemann, T., Winkelstern, I., Yarian, D., Yoshida, N., Zhang, N., Ziegler, M., 2021. InterCarb: A community effort to improve interlaboratory standardization of the carbonate

clumped isotope thermometer using carbonate standards. Geochem. Geophys. Geosyst. 22.
Brand, W.A., Assonov, S.S., Coplen, T.B., 2010. Correction for the ^{17}O interference in $\delta(^{13}C)$ measurements when analyzing CO_2 with stable isotope mass spectrometry (IUPAC Technical Report). Pure Appl. Chem. 82, 1719–1733.
Burns, S.J., Fleitmann, D., Matter, A., Kramers, J., Al-Subbary, A.A., 2003. Indian Ocean Climate and an Absolute Chronology over Dansgaard/Oeschger Events 9 to 13. Science 301, 1365–1367.
Carpenter, S.J., Lohmann, K.C., 1995. $\delta^{18}O$ and $\delta^{13}C$ values of modern brachiopod shells. Geochim. Cosmochim.Acta 59, 3749–3764.
Cohen, A.L., 2003. Geochemical perspectives on coral mineralization. Rev. Mineral. Geochem. 54, 151–187.
Craig, H. and Gordon, L.I., 1965. Deuterium and oxygen 18 variations in the ocean and the marine atmosphere.277-274.
Daëron, M., Guo, W., Eiler, J., Genty, D., Blamart, D., Boch, R., Drysdale, R., Maire, R., Wainer, K., Zanchetta, G., 2011. $^{13}C^{18}O$ clumping in speleothems: Observations from natural caves and precipitation experiments. Geochim. Cosmochim. Acta 75, 3303–3317.
Daëron, M., Blamart, D., Peral, M., Affek, H.P., 2016. Absolute isotopic abundance ratios and the accuracy of Δ_{47} measurements. Chem. Geol. 442, 83–96.
Daëron, M., Drysdale, R.N., Peral, M., Huyghe, D., Blamart, D., Coplen, T.B., Lartaud, F., Zanchetta, G., 2019. Most Earth-surface calcites precipitate out of isotopic equilibrium. Nat. Commun. 10, 429.
Dansgaard, W., 1964. Stable isotopes in precipitation. Tellus Dyn. Meteorol. Oceanogr. 16, 436.
Day, C.C., Henderson, G.M., 2011. Oxygen isotopes in calcite grown under cave-analogue conditions. Geochim. Cosmochim. Acta 75, 3956–3972.
Dennis, K.J., Affek, H.P., Passey, B.H., Schrag, D.P., Eiler, J.M., 2011. Defining an absolute reference frame for 'clumped' isotope studies of CO_2. Geochim. Cosmochim. Acta 75, 7117–7131.
Dorale, J., Liu, Z., 2009. Limitations of hendy test criteria in judging the paleoclimatic suitability of speleothems and the need for replication. J. Cave Karst Stud. 71, 73–80.
Dreybrodt, W., 2012. Processes in Karst Systems: Physics, Chemistry, andGeology. Springer Science & Business Media.
Dreybrodt, W., Hansen, M., Scholz, D., 2016. Processes affecting the stable isotope composition of calcite during precipitation on the surface of stalagmites: Laboratory experiments investigating the isotope exchange between DIC in the solution layer on top of a speleothem and the CO_2 of the cave atmosphere. Geochim. Cosmochim. Acta 174, 247–262.
Dreybrodt, W., Scholz, D., 2011. Climatic dependence of stable carbon and oxygen isotope signals recorded in speleothems: From soil water to speleothem calcite. Geochim. Cosmochim. Acta 75, 734–752.
Eiler, J.M., 2007. "Clumped-isotope" geochemistry—The study of naturally-occurring, multiply-substituted isotopologues. Earth Planet. Sci. Lett. 262, 309–327.
Eiler, J.M., Schauble, E., 2004. $^{18}O^{13}C^{16}O$ in Earth's atmosphere. Geochim. Cosmochim. Acta 68, 4767–4777.
El-Shenawy, M.I., Kim, S.-T., Schwarcz, H.P., 2020. Carbon and oxygen isotope systematics in cave environments: Lessons from an artificial cave "McMaster Cave". Geochim. Cosmochim. Acta 272, 137–159.
Falk, E.S., Guo, W., Paukert, A.N., Matter, J.M., Mervine, E.M., Kelemen, P.B., 2016. Controls on the stable isotope compositions of travertine from hyperalkaline springs in Oman: Insights from clumped isotope measurements. Geochim. Cosmochim. Acta 192, 1–28.
Fiebig, J., Bajnai, D., Löffler, N., Methner, K., Krsnik, E., Mulch, A., Hofmann, S., 2019. Combined high-precision Δ_{48} and Δ_{47} analysis of carbonates. Chem. Geol. 522, 186–191.
Fiebig, J., Daëron, M., Bernecker, M., Guo, W., Schneider, G., Boch, R., Bernasconi, S.M., Jautzy, J., Dietzel, M., 2021. Calibration of the dual clumped isotope thermometer for carbonates. Geochim. Cosmochim.Acta. S0016703721004208.
Fleitmann, D., Burns, S.J., Mudelsee, M., Neff, U., Kramers, J., Mangini, A., Matter, A., 2003. Holocene Forcing of the Indian Monsoon Recorded in a Stalagmite from Southern Oman. Science 300, 1737–1739.
Ghadiri, E., Vogel, N., Brennwald, M.S., Maden, C., Häuselmann, A.D., Fleitmann, D., Cheng, H., Kipfer, R., 2018. Noble gas based temperature reconstruction on a Swiss stalagmite from the last glacial–interglacial transition and its comparison with other climate records. Earth Planet. Sci. Lett. 495, 192–201.
Ghosh, P., Adkins, J., Affek, H., Balta, B., Guo, W., Schauble, E.A., Schrag, D., Eiler, J.M., 2006. ^{13}C–^{18}O bonds in carbonate minerals: A new kind of paleothermometer. Geochim. Cosmochim. Acta 70, 1439–1456.
Griffiths, M.L., Johnson, K.R., Pausata, F.S.R., White, J.C., Henderson, G.M., Wood, C.T., Yang, H., Ersek, V., Conrad, C., Sekhon, N., 2020. End of Green Sahara amplified mid- to late Holocene megadroughts in mainland Southeast Asia. Nat. Commun. 11, 4204.
Guo, W., 2020. Kinetic clumped isotope fractionation in the DIC-H_2O-CO_2 system: Patterns, controls, and implications. Geochim. Cosmochim. Acta 268, 230–257.
Guo, W., Mosenfelder, J.L., Goddard III, W.A., Eiler, J.M., 2009. Isotopic fractionations associated with phosphoric acid digestion of carbonate minerals: Insights from first-princliples theoretical modeling and clumped isotope measurements. Geochim. Cosmochim. Acta 73 (24), 7203–7225.
Guo, W., Zhou, C., 2019. Patterns and controls of disequilibrium isotope effects in speleothems: Insights from an isotope-enabled diffusion-reaction model and implications for quantitative thermometry. Geochim. Cosmochim.Acta 267, 196–226.
Hansen, M., Dreybrodt, W., Scholz, D., 2013. Chemical evolution of dissolved inorganic carbon species flowing in thin water films and its implications for (rapid) degassing of CO_2 during speleothem growth. Geochim. Cosmochim. Acta 107, 242–251.
Hansen, M., Kluge, T., Scholz, D., 2022. Investigation of disequilibrium clumped isotope fractionation in (speleothem) $CaCO_3$ with cave analogous laboratory experiments using thin films of flowing solution. Geochim. Cosmochim. Acta 321, 244–264.
Hansen, M., Scholz, D., Froeschmann, M.-L., Schöne, B.R., Spötl, C., 2017. Carbon isotope exchange between gaseous CO_2 and thin solution films: Artificial cave experiments and a complete diffusion-reaction model. Geochim. Cosmochim. Acta 211, 28–47.
Hansen, M., Scholz, D., Schöne, B.R., Spötl, C., 2019. Simulating speleothem growth in the laboratory: Determination of the stable isotope fractionation ($\delta^{13}C$ and $\delta^{18}O$) between H_2O, DIC and $CaCO_3$. Chem. Geol. 509, 20–44.
Hendy, C.H., 1971. The isotopic geochemistry of speleothems—I. The calculation of the effects of different modes of formation on the isotopic composition of speleothems and their applicability as palaeoclimatic indicators. Geochim. Cosmochim. Acta 35, 801–824.
Hill, P.S., Tripati, A.K., Schauble, E.A., 2014. Theoretical constraints on the effects of pH, salinity, and temperature on clumped isotope signatures of dissolved inorganic carbon species and precipitating carbonate minerals. Geochim. Cosmochim. Acta 125, 610–652.
John, C.M., Bowen, D., 2016. Community software for challenging isotope analysis: First applications of 'Easotope' to clumped isotopes: Community software for challenging isotope analysis. Rapid Commun. Mass Spectrom. 30, 2285–2300.
Johnston, V.E., Borsato, A., Spötl, C., Frisia, S., Miorandi, R., 2013. Stable isotopes in caves over altitudinal gradients: fractionation behaviour and inferences for speleothemsensitivity to climate change. Clim. Past 9, 99–118.
Kim, S.-T., O'Neil, J.R., 1997. Equilibrium and nonequilibrium oxygen isotope effects in synthetic carbonates. Geochim. Cosmochim. Acta 61, 3461–3475.
Kimball, J., Eagle, R., Dunbar, R., 2016. Carbonate "clumped" isotope signatures in aragonitic scleractinian and calcitic gorgonian deep-sea corals. Biogeosciences 13, 6487–6505.
Kluge, T., Affek, H.P., 2012. Quantifying kinetic fractionation in Bunker Cave speleothems using Δ_{47}. Quat. Sci. Rev. 49, 82–94.
Kluge, T., Marx, T., Scholz, D., Niggemann, S., Mangini, A., Aeschbach-Hertig, W., 2008. A new tool for palaeoclimate reconstruction: Noble gas temperatures from fluid inclusions in speleothems. Earth Planet. Sci. Lett. 269, 408–415.
Kluge, T., Affek, H.P., Marx, T., Aeschbach-Hertig, W., Riechelmann, D.F.C., Scholz, D., Riechelmann, S., Immenhauser, A., Richter, D.K., Fohlmeister, J., Wackerbarth, A., Mangini, A., Spötl, C., 2013. Reconstruction of drip-water $\delta^{18}O$ based on calcite oxygen and clumped isotopes of speleothems from Bunker Cave (Germany). Clim. Past 9, 377–391.
Kluge, T., Affek, H.P., Dublyansky, Y., Spötl, C., 2014. Devils Hole paleotemperatures and implications for oxygen isotope equilibrium fractionation. Earth Planet. Sci. Lett. 400, 251–260.
Kovacs, S.E., Reinhardt, E.G., Werner, C., Kim, S.-T., Devos, F., Le Maillot, C., 2018. Seasonal trends in calcite-raft precipitation from cenotes Rainbow, Feno and Monkey Dust, Quintana Roo, Mexico: Implications for paleoenvironmental studies. Palaeogeogr. Palaeoclimatol. Palaeoecol. 497, 157–167.
Krüger, Y., Marti, D., Staub, R.H., Fleitmann, D., Frenz, M., 2011. Liquid–vapour homogenisation of fluid inclusions in stalagmites: Evaluation of a new thermometer for palaeoclimate research. Chem. Geol. 289, 39–47.
Lachniet, M.S., 2009. Climatic and environmental controls on speleothem oxygen-isotope values. Quat. Sci. Rev. 28, 412–432.
Lucarelli, J.K., Carroll, H.M., Ulrich, R.N., Elliott, B.M., Coplen, T.B., Eagle, R.A., Tripati, A., 2023a. Equilibrated Gas and Carbonate Standard-Derived Dual (Δ_{47} and Δ_{48}) Clumped Isotope Values. Geochem. Geophys. Geosystems 24, e2022GC010458.
Lucarelli, J.K., Purgstaller, B., Ulrich, R.N., Parvez, Z., Leis, A., Goetschl, K.E., Eagle, R. A., Dietzel, M., Tripati, A., 2023b. Dual clumped (Δ_{47}-Δ_{48}) isotope data for amorphous carbonates and transformation products reveal a novel mechanism for disequilibrium clumped isotope effects. Geochim. Cosmochim. Acta 359, 119–134.
Matthews, A., Affek, H.P., Ayalon, A., Vonhof, H.B., Bar-Matthews, M., 2021. Eastern Mediterranean climate change deduced from the Soreq Cave fluid inclusion stable isotopes and carbonate clumped isotopes record of the last 160 ka. Quat. Sci. Rev. 272, 107223.
McConnaughey, T., 1989. ^{13}C and ^{18}O isotopic disequilibrium in biological carbonates: II. In vitro simulation of kinetic isotope effects. Geochim. Cosmochim. Acta 53, 163–171.
McDermott, F., 2004. Palaeo-climate reconstruction from stable isotope variations in speleothems: a review. Quat. Sci. Rev. 23, 901–918.
McDermott, F., Atkinson, T.C., Fairchild, I.J., Baldini, L.M., Mattey, D.P., 2011. A first evaluation of the spatial gradients in $\delta^{18}O$ recorded by European Holocene speleothems. Glob. Planet. Change 79, 275–287.
McDermott, F., Schwarcz, H., Rowe, P.J., 2006. Isotopes in speleothems (185-225). Springer Netherlands.
Meckler, A.N., Affolter, S., Dublyansky, Y.V., Krüger, Y., Vogel, N., Bernasconi, S.M., Frenz, M., Kipfer, R., Leuenberger, M., Spötl, C., Carolin, S., Cobb, K.M., Moerman, J., Adkins, J.F., Fleitmann, D., 2015. Glacial–interglacial temperature change in the tropical West Pacific: A comparison of stalagmite-based paleo-thermometers. Quat. Sci. Rev. 127, 90–116.
Mickler, P.J., Banner, J.L., Stern, L., Asmerom, Y., Edwards, R.L., Ito, E., 2004. Stable isotope variations in modern tropical speleothems: Evaluating equilibrium vs. kinetic isotope effects. Geochim. Cosmochim. Acta 68, 4381–4393.
Mickler, P.J., Stern, L.A., Banner, J.L., 2006. Large kinetic isotope effects in modern speleothems. Geol. Soc. Am. Bull. 118, 65–81.
Mühlinghaus, C., Scholz, D., Mangini, A., 2009. Modelling fractionation of stable isotopes in stalagmites. Geochim. Cosmochim. Acta 73, 7275–7289.

Oster, J.L., Montañez, I.P., Sharp, W.D., Cooper, K.M., 2009. Late Pleistocene California droughts during deglaciation and Arctic warming. Earth Planet. Sci. Lett. 288, 434–443.

Parvez, Z.A., Lucarelli, J.K., Matamoros, I.W., Rubi, J., Miguel, K., Elliott, B., Flores, R., Ulrich, R.N., Eagle, R.A., Watkins, J.M., Christensen, J.N., 2023. Dual carbonate clumped isotopes (Δ_{47}-Δ_{48}) constrains kinetic effects and timescales in peridotite-associated springs at The Cedars, Northern California. Geochim. Cosmochim. 358, 77–92.

Poulson, T.L., White, W.B., 1969. The Cave Environment: Limestone caves provide unique natural laboratories for studying biological and geological processes. Science 165, 971–981.

Powers, L.A., Werne, J.P., Johnson, T.C., Hopmans, E.C., Sinninghe Damsté, J.S., Schouten, S., 2004. Crenarchaeotal membrane lipids in lake sediments: A new paleotemperature proxy for continental paleoclimate reconstruction? Geology 32, 613.

Richards, D.A., 2003. Uranium-series Chronology and Environmental Applications of Speleothems. Rev. Mineral. Geochem. 52, 407–460.

Rollion-Bard, C., Blamart, D., Cuif, J.-P., Dauphin, Y., 2010. In situ measurements of oxygen isotopic composition in deep-sea coral, Lophelia pertusa: Re-examination of the current geochemical models of biomineralization. Geochim. Cosmochim. Acta 74, 1338–1349.

Rollion-Bard, C., Milner, G.S., Burckel, P., Angiolini, L., Jurikova, H., Tomašových, A., Henkel, D., 2019. Assessing the biomineralization processes in the shell layers of modern brachiopods from oxygen isotopic composition and elemental ratios: Implications for their use as paleoenvironmental proxies. Chem. Geol. 524, 49–66.

Saenger, C., Affek, H.P., Felis, T., Thiagarajan, N., Lough, J.M., Holcomb, M., 2012. Carbonate clumped isotope variability in shallow water corals: Temperature dependence and growth-related vital effects. Geochim. Cosmochim. Acta 99, 224–242.

Schauble, E.A., Ghosh, P., Eiler, J.M., 2006. Preferential formation of ^{13}C–^{18}O bonds in carbonate minerals, estimated using first-principles lattice dynamics. Geochim. Cosmochim. Acta 70, 2510–2529.

Scheidegger, Y., Brennwald, M.S., Fleitmann, D., Jeannin, P.-Y., Wieler, R., Kipfer, R., 2011. Determination of Holocene cave temperatures from Kr and Xe concentrations in stalagmite fluidinclusions. Chem. Geol. 288, 61–66.

Scholz, D., Hoffmann, D., 2008. ^{230}Th/U-dating of fossil corals and speleothems. Quat. Sci. J. 57, 52–76.

Serrato, G., 2020. Investigating Mexican paleoclimate with precisely dated speleothems. Doctoral dissertation. Massachusetts Institute of Technology.

Serrato Marks, G., Medina-Elizalde, M., Burns, S., Weldeab, S., Lases-Hernandez, F., Cazares, G., McGee, D., 2021. Evidence for Decreased Precipitation Variability in the Yacatan Peninsula During the Mid-Holocene. Paleooceanogr. Paleoclimatol. 36 (5), e2021PA004219.

Spooner, P.T., Guo, W., Robinson, L.F., Thiagarajan, N., Hendry, K.R., Rosenheim, B.E., Leng, M.J., 2016. Clumped isotope composition of cold-water corals: A role for vital effects? Geochim. Cosmochim. Acta 179, 123–141.

Swart, P.K., Lu, C., Moore, E.W., Smith, M.E., Murray, S.T., Staudigel, P.T., 2021. A calibration equation between Δ_{48} values of carbonate and temperature. Rapid communications in mass spectrometry 35 (17), e9147.

Tang, K., Feng, X., 2001. The effect of soil hydrology on the oxygen and hydrogen isotopic compositions of plants' source water. Earth Planet. Sci. Lett. 185, 355–367.

Thiagarajan, N., Adkins, J., Eiler, J., 2011. Carbonate clumped isotope thermometry of deep-sea corals and implications for vital effects. Geochim. Cosmochim. Acta 75, 4416–4425.

Tierney, J.E., Russell, J.M., Huang, Y., Damsté, J.S.S., Hopmans, E.C., Cohen, A.S., 2008. Northern hemisphere controls on tropical Southeast African climate during the past 60,000years. Science 322, 252–255.

Tremaine, D.M., Froelich, P.N., Wang, Y., 2011. Speleothem calcite farmed in situ: Modern calibration of $\delta^{18}O$ and $\delta^{13}C$ paleoclimate proxies in a continuously-monitored natural cave system. Geochim. Cosmochim. Acta 75, 4929–4950.

Tripati, A.K., Hill, P.S., Eagle, R.A., Mosenfelder, J.L., Tang, J., Schauble, E.A., Eiler, J. M., Zeebe, R.E., Uchikawa, J., Coplen, T.B., Ries, J.B., Henry, D., 2015. Beyond temperature: Clumped isotope signatures in dissolved inorganic carbon species and the influence of solution chemistry on carbonate mineral composition. Geochim. Cosmochim. Acta 166, 344–371.

Uchikawa, J., Chen, S., Eiler, J.M., Adkins, J.F., Zeebe, R.E., 2021. Trajectory and timescale of oxygen and clumped isotope equilibration in the dissolved carbonate system under normal and enzymatically-catalyzed conditions at 25 C. Geochim. Cosmochim. Acta 314, 313–333.

Upadhyay, D., Lucarelli, J., Arnold, A., Flores, R., Bricker, H., Ulrich, R.N., Jesmok, G., Santi, L., Defliese, W., Eagle, R.A., Carroll, H.M., Bateman, J.B., Petryshyn, V., Loyd, S.J., Tang, J., Priyadarshi, A., Elliott, B., Tripati, A., 2021. Carbonate clumped isotope analysis (Δ_{47}) of 21 carbonate standards determined via gas-source isotope-ratio mass spectrometry on four instrumental configurations using carbonate-based standardization and multiyear data sets. Rapid Commun. Mass Spectrom 35.

Van Breukelen, M.R., Vonhof, H.B., Hellstrom, J.C., Wester, W.C.G., Kroon, D., 2008. Fossil dripwater in stalagmites reveals Holocene temperature and rainfall variation in Amazonia. Earth Planet. Sci. Lett. 275, 54–60.

Wang, X., Auler, A.S., Edwards, R.L., Cheng, H., Cristalli, P.S., Smart, P.L., Richards, D. A., Shen, C.-C., 2004a. Wet periods in northeastern Brazil over the past 210 kyr linked to distant climate anomalies. Nature 432, 740–743.

Wang, Y.J., Cheng, H., Edwards, R.L., An, Z.S., Wu, J.Y., Shen, C.C., Dorale, J.A., 2001. A high-resolution absolute-dated late Pleistocene monsoon record from Hulu Cave, China. Science 294 (5550), 2345–2348.

Wang, J.K., Johnson, K.R., Borsato, A., Amaya, D.J., Griffiths, M.L., Henderson, G.M., Frisia, S., Mason, A., 2019. Hydroclimatic variability in Southeast Asia over the past two millennia. Earth Planet. Sci. Lett. 525, 115737.

Wang, Z., Schauble, E.A., Eiler, J.M., 2004b. Equilibrium thermodynamics of multiply substituted isotopologues of molecular gases. Geochim. Cosmochim. Acta 68, 4779–4797.

Watkins, J.M., Devriendt, L.S., 2022. A combined model for kinetic clumped isotope effects in the $CaCO_3$-DIC-H_2O system. Geochem. Geophys. Geosyst. 23 (8), e2021GC010200.

Wortham, B.E., Montañez, I.P., Bowman, K., Kuta, D., Contreras, N.S., Brummage, E., Pang, A., Tinsley, J., Roemer-Baer, G., 2021. Monitoring of Sierra Nevada Caves Reveals the Potential for Stalagmites to Archive Seasonal Variability. Front. Earth Sci. 9, 781526.

Wright, K.T., Johnson, K.R., Bhattacharya, T., Marks, G.S., McGee, D., Elsbury, D., Peings, Y., Lacaille-Muzquiz, J., Lum, G., Beramendi-Orosco, L., Magnusdottir, G., 2022. Precipitation in Northeast Mexico primarily controlled by the relative warming of Atlantic SSTs. Geophys. Res. Lett. 49, e2022GL098186.

Zeebe, R.E., Wolf-Gladrow, D.A., 2001. CO_2 in Seawater: Equilibrium, Kinetics, Isotopes. Elsevier, Amsterdam, New York.